Atmos. Chem. Phys., 26, 8475–8504, 2026
https://doi.org/10.5194/acp-26-8475-2026

Atmospheric Chemistry and Physics
Open Access
EGU

Research article

Active and passive satellite observations coupled with carbon–nitrogen synergy for urban fossil fuel CO_2 emissions monitoring

Jinchun Yi[1,★], Yiyang Huang[1,★], Ge Han[1,3], Hongyuan Zhang[2], Zhipeng Pei[1,3], Haotian Luo[1], Yichi Zhang[1], Tianqi Shi[6], Siwei Li[1,3], and Wei Gong[4,5]

[1]Hubei Key Laboratory of Quantitative Remote Sensing of Land and Atmosphere, School of Remote Sensing and Information Engineering, Wuhan University, Wuhan 430079, China
[2]State Key Laboratory of Information Engineering in Surveying, Mapping and Remote Sensing, Wuhan University, Luoyu Road No.129, Wuhan 430079, China
[3]Perception and Effectiveness Assessment for Carbon-neutrality Efforts, Engineering Research Center of Ministry of Education, Institute for Carbon Neutrality, Wuhan University, Wuhan, China
[4]Electronic Information School, Wuhan University, Wuhan, China
[5]Wuhan Institute of Quantum Technology, Wuhan, China
[6]Laboratoire des Sciences du Climat et de l'Environnement, LSCE/IPSL, CEA-CNRS-UVSQ, Université Paris-Saclay, 91198 Gif-sur-Yvette, France
★These authors contributed equally to this work.

Correspondence: Ge Han (udhan@whu.edu.cn)

Received: 29 January 2026 – Discussion started: 12 February 2026
Revised: 2 June 2026 – Accepted: 3 June 2026 – Published: 17 June 2026

Abstract. Accurate estimation of fossil fuel CO_2 ($ffCO_2$) emissions is essential for climate prediction and the development of mitigation policies. Top-down carbon–nitrogen joint observations offer the potential for more reliable $ffCO_2$ estimates. Here, we establish an inversion framework for urban $ffCO_2$ emissions based on combined active–passive satellite observations. Urban $ffCO_2$ distributions were first constructed using satellite NO_2 data and CO_2–NO_x emission ratios, and monthly $ffCO_2$ emissions for selected global cities were then estimated by integrating the total column dry-air carbon dioxide (XCO_2) from the DQ-1 ACDL instrument. Our results show that satellite-derived NO_x emissions provide strong constraints on urban anthropogenic CO_2 estimates. Validation against TCCON ground-based observations indicates that, compared with conventional top-down inversion approaches, our method more accurately reproduces urban $ffXCO_2$ plume distributions. We further evaluated the influence of different CO_2–NO_x ratio calculation methods on $ffCO_2$ estimates and found variations exceeding 150, exerting a substantial impact on emission inversions. Under observational constraints, the uncertainty in CO_2–NO_x ratios derived from different methods decreased by 9.79 %–38.78 %, and the variation range was reduced by more than 100 %, converging toward a consistent magnitude. This study advances understanding of the spatiotemporal patterns of urban $ffCO_2$ emissions and provides a unified perspective for future CO_2–NO_x-based anthropogenic carbon emission estimation.

Published by Copernicus Publications on behalf of the European Geosciences Union.

1 Introduction

The intensification of global climate change has driven an increasing demand for high-precision monitoring of fossil fuel CO_2 ($ffCO_2$) emissions (Agency, 2009). The Paris Agreement emphasizes that countries need rapid and timely access to changes in carbon emissions to support policy formulation and implementation. Achieving this goal relies on accurate and verifiable carbon accounting systems. Cities, due to their high concentration of population, energy consumption, and economic activity, contribute over 70 % of global anthropogenic CO_2 emissions, making them key units for evaluating emission reduction policies and compliance monitoring (Crippa et al., 2018). Existing global and regional emission inventories primarily adopt bottom-up statistical accounting methods, estimating emissions based on energy production and sector-specific emission factors (Xu et al., 2024; Wei, 2024). However, these inventories often suffer from significant uncertainties due to data delays and incompleteness (Le Quéré et al., 2018).

To overcome the limitations of bottom-up approaches, top-down atmospheric inversion techniques have advanced rapidly in recent years, enabling constraints on regional carbon budgets. Passive satellite remote sensing systems, such as GOSAT and OCO-2/3, can invert XCO_2 over large portions of the globe and have unique potential for identifying local point sources, estimating regional carbon fluxes, and inferring gross primary productivity (Schwandner et al., 2017; Eldering et al., 2017; Sun et al., 2018b). Nonetheless, top-down inversion methods also rely on accurate prior emission estimates. Inventories that downscale national or regional emissions to high spatial and temporal resolution often suffer from incomplete socio-economic data and inaccurate emission conversion factors, leading to substantial uncertainties in urban emission estimates (Xing et al., 2025; Xu et al., 2025a). Moreover, conventional top-down CO_2 inversion studies have focused primarily on quantifying terrestrial ecosystem carbon fluxes, typically assuming fossil fuel emissions are known and unbiased (Pei et al., 2022). This complicates direct inference of anthropogenic emissions from CO_2 observations due to the atmospheric mixing of fossil fuel and ecosystem fluxes (Ye et al., 2020).

Coupled carbon-nitrogen observations offer a new perspective to address this gap (Reuter et al., 2019; Yang et al., 2023). Nitrogen oxides ($NO_x = NO + NO_2$) are major co-emitted species from fossil fuel combustion, with emission intensity and spatial distribution closely correlated with $ffCO_2$ (Feng et al., 2024). Studies have shown that in regions with varying pollution levels, XCO_2 anomalies spatially correlate with tropospheric NO_2 column densities (Hakkarainen et al., 2016). Moreover, the CO_2-to-NO_x ratio is often more stable than individual emission amounts because systematic biases in fossil fuel consumption affect both CO_2 and NO_x statistics (Konovalov et al., 2016). Recent research suggests that optimized NO_x emissions, combined with CO_2-to-NO_x ratios from bottom-up inventories, can provide more accurate $ffCO_2$ estimates (Zheng et al., 2020). For instance, Zheng et al. used TROPOMI NO_2 data to estimate 10 d moving averages of Chinese $ffCO_2$ emissions during the COVID-19 pandemic, finding an 11.5 % decline compared to the same period in 2019 (Zheng et al., 2020). Liu et al. (2020) validated the feasibility of NO_x-based $ffCO_2$ estimation by comparing inferred CO_2 emissions with highly accurate stack measurements from eight large US power plant. High-resolution NO_2 column observations, such as those from Sentinel-5P/TROPOMI, can be inverted using a mass-balance framework to derive accurate NO_x gridded fluxes (Qin et al., 2023; Sun, 2022). These NO_x fluxes can inform the prior spatial allocation of CO_2 emissions due to the co-emission consistency of fossil fuel sources, and the high temporal resolution of TROPOMI allows rapid updates of CO_2 priors, mitigating the lag inherent in static inventories (Zhang et al., 2022).

The CO_2-to-NO_x ratio is crucial for converting NO_x emissions into $ffCO_2$ estimates. However, because the CO_2-to-NO_x ratio used in this study is calculated from CO_2 emissions and NO_x emissions, there is currently a lack of accurate top-down measurement methods, most studies derive this ratio from inventories, and different calculation methods yield significantly different values. Assimilating observational data to invert CO_2-to-NO_x ratios is therefore key to reducing uncertainties in $ffCO_2$ estimation. Passive top-down observations are limited by cloud cover, aerosols, and solar irradiance, and in complex multi-source and topographic environments, signal attribution is challenging, restricting the accuracy and stability of city-scale inversions (Miller et al., 2014; Han et al., 2026).

In 2022, China launched DQ-1, the world's first CO_2 lidar satellite, equipped with an IPDA lidar (ACDL) capable of high signal-to-noise ratio, day-and-night, all-weather observations. The dual-wavelength differential method mitigates interference from aerosols and thin clouds (Han et al., 2025). Compared to passive satellites, IPDA lidar offers unique advantages in urban plume detection and fine-scale emission inversion (Kiemle et al., 2017; Zhang et al., 2026). Previous studies using DQ-1 XCO_2 data successfully constrained point-source emissions (Cheng et al., 2025; Han et al., 2024; Zhang et al., 2025), and Yi et al. developed a kilometer-scale urban flux inversion system based on ACDL measurements, comparing its constraints to passive systems like OCO-2/3 (Yi et al., 2025b).

In this study, we propose a city-scale $ffCO_2$ inversion framework that jointly assimilates active and passive satellite observations, dynamically bridging NO_x and CO_2 emissions via the CO_2-to-NO_x ratio. The workflow is illustrated in Fig. 1. TROPOMI NO_2 column data are first used to invert NO_x gridded emissions via a mass-balance approach. Combined with prior CO_2-to-NO_x ratios, these NO_x fluxes are converted into CO_2 priors. DQ-1 XCO_2-Lidar along-track measurements are then assimilated using WRF-STILT

high-resolution atmospheric transport simulations within a Bayesian inversion framework to estimate total city emissions and explicitly quantify observational and transport uncertainties. We applied this approach to Beijing, Paris, and Cairo, representing cities with diverse topographies and emission patterns, using August 2022 TROPOMI and DQ-1/ACDL data to evaluate the framework's ability to provide robust, high-resolution urban emission estimates. It is noteworthy that no unified CO_2-to-NO_x ratio calculation method currently exists, and different methods yield divergent values, which can significantly bias final emission estimates. This study systematically evaluates the influence of prior CO_2-to-NO_x ratio calculation methods on inversion outcomes, demonstrating that Bayesian assimilation can substantially reduce this uncertainty, converging different ratios to a consistent magnitude. This framework offers a unified approach for estimating urban emissions under limited or uncertain inventory conditions, providing a timely and reliable method for reporting anthropogenic CO_2 emissions at the city scale.

The remainder of this paper is structured as follows. Section 2 introduces the datasets and methods used in this study. Section 3 presents the results of NO_x emission estimation in Paris, Cairo, and Beijing based on TROPOMI observations combined with a mass-balance approach, followed by city-scale $ffCO_2$ inversion results obtained by assimilating DQ-1 ACDL observations within a Bayesian framework. Section 4 examines the influence of different prior CO_2-to-NO_x ratio calculation methods on the inversion process and highlights the importance of optimizing the CO_2-to-NO_x ratio using observational data. Finally, Sect. 5 summarizes and discusses the potential of the multi-source satellite Bayesian inversion framework for constraining urban CO_2 emissions, and emphasizes the significance of optimized CO_2-to-NO_x ratios for improving the accuracy of urban $ffCO_2$ estimates.

2 Materials and methods

2.1 Data

2.1.1 ACDL Productions

The concept of DQ-1 was first proposed in 2012 with the aim of developing a satellite-borne lidar system analogous to the Cloud-Aerosol Lidar with Orthogonal Polarization (CALIOP) onboard CALIPSO, and it was officially approved as a national project in 2017 (Zhang et al., 2024). Unlike conventional environmental monitoring satellites, DQ-1 is distinguished by its breakthrough active remote sensing payload – the Atmospheric Carbon Dioxide Differential Absorption Lidar (ACDL) – which enables active "top-down" observations of atmospheric CO_2 (Zhang et al., 2023). The ACDL underwent successive stages of laboratory prototype development and airborne validation before its successful launch onboard the DQ-1 satellite into a near-polar sun-synchronous orbit at an altitude of ~ 705 km on 18 April 2022. Operational observations commenced in late May of the same year. This study primarily analyzes data collected August 2022.

The ACDL operates on the principle of Integrated Path Differential Absorption (IPDA) lidar, retrieving atmospheric column-averaged CO_2 concentrations (XCO_2) via differential absorption techniques. The inversion methodology and data product specifications have been described in detail elsewhere; here, we provide only a brief overview (Han et al., 2025). The instrument transmits two nearly simultaneous laser pulses: one at a strong absorption line of CO_2 (R16, referred to as the "online" wavelength) and the other at a nearby weak absorption line (the "offline" wavelength). These are stabilized at 6361.225 and 6360.981 cm^{-1}, corresponding to 1572.024 and 1572.085 nm, respectively. By comparing the differential attenuation between the online and offline signals, the system effectively mitigates the influence of aerosols and other interfering species, except water vapor, thereby enabling accurate retrievals of XCO_2. The inversion process relies on dedicated algorithms, with the central concept being that the small wavelength offset produces differential absorption, which enhances the sensitivity of CO_2 detection (details of the ACDL XCO_2 retrieval algorithm are provided in the Appendix A1).

Figure 2 illustrates the schematic of the DQ-1 measurement principle. The XCO_2 products generated by ACDL are provided in a point-sampling mode analogous to that of GOSAT. The lidar records one footprint of approximately 70 m every ~ 350 m along the satellite ground track. Additional details of the ACDL operating parameters are provided in the Appendix A1.

2.1.2 TROPOMI Productions

TROPOMI is a nadir-viewing spectrometer onboard ESA's Sentinel-5 Precursor (S5P) satellite, which was launched in October 2017. Operating in an ascending Sun-synchronous polar orbit with an equator crossing time of approximately 13:30 local time, TROPOMI measures a range of trace gases as well as cloud and aerosol properties across four spectral channels (ultraviolet, visible, near-infrared, and shortwave infrared). The instrument's minimum pixel size was about $3.5 \times 7\,km^2$ at nadir before being reduced to $\sim 3.5 \times 5.5\,km^2$ on 6 August 2019 (Veefkind et al., 2012). In this study, we used the S5P-PAL dataset (consistent with version 2.3.1) covering the period from 1 August–1 September 2022, obtained from https://data-portal.s5p-pal.com (last access: 29 January 2026).

To ensure data quality, we filtered out pixels with a qa_value < 0.75 (Qin et al., 2023), and, following van Geffen et al., removed cloudy pixels (cloud radiance fraction $> 50\,\%$) as well as anomalies (e.g., eclipses) from the TROPOMI NO_2 dataset (Van Geffen et al., 2022). To test our algorithm framework on a robust dataset, we selected summer NO_2 observations for three cities located in the mid-

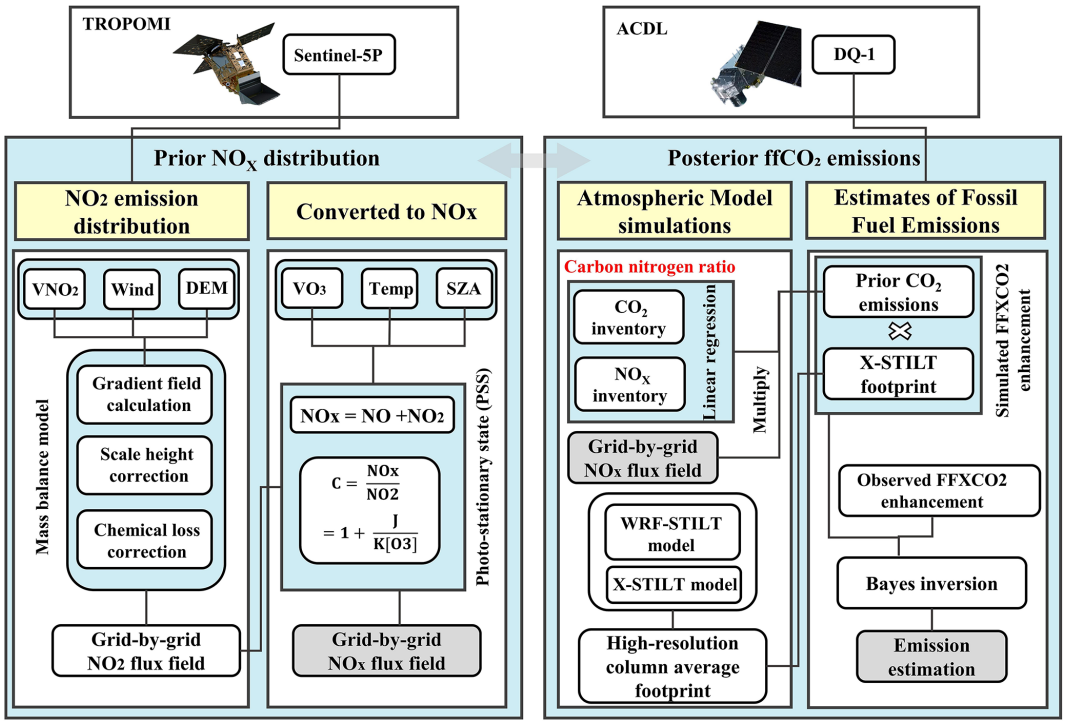

Figure 1. Technical framework diagram.

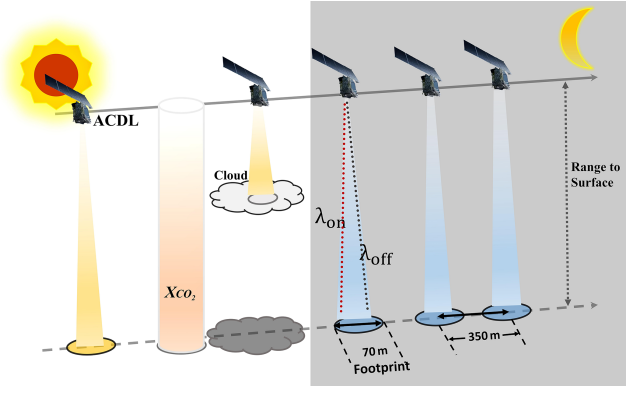

Figure 2. the schematic diagram for DQ-1's detection principle.

latitudes of the Northern Hemisphere, avoiding winter measurements that may be complicated by potential snow cover. Furthermore, given the need for city-scale accuracy, air mass factor (AMF) corrections were applied locally following the method described in Beirle et al. (2023).

Sun et al. proposed an oversampling algorithm to project multi-satellite, multi-species observations onto a common grid, with code publicly available on GitHub (https://github.com/Kang-Sun-CfA/Oversampling_matlab/, last access: 29 January 2026) (Sun et al., 2018a). In this work, we applied this algorithm to the pre-processed TROPOMI overpass data, generating oversampled grids at 1 km resolution following the procedure described in Sun (2022).

2.1.3 Meteorological and DEM data

For the estimation of CO_2 emissions through model simulations, we utilized meteorological parameters from the National Centers for Environmental Prediction Final (NCEP FNL) operational global analysis dataset. The ds083.3 dataset is provided on a $0.25° \times 0.25°$ latitude–longitude grid and updated every six hours via the Global Data Assimilation System (GDAS) (https://rda.ucar.edu/datasets/ds083-3/, last access: 29 January 2026). It covers 32 vertical levels, ranging from the surface to the top of the atmosphere, including the ground level and 31 isobaric layers from 1000–1 hPa. Essential variables such as surface pressure, geopotential height, temperature, relative humidity, and zonal and meridional wind components were used as the main meteorological inputs for driving the WRF-STILT simulations.

The wind vector data were obtained from the ERA5 reanalysis dataset (https://doi.org/10.24381/cds.adbb2d47) (Hersbach et al., 2023). We extracted hourly 10 and 100 m wind vectors at 0.25° spatial resolution for the three selected cities during the period from 1 August–1 September 2022. The 10 m wind vectors are used to approximate near-surface winds, whereas the 100 m wind vectors represent horizontal transport within the planetary boundary layer. These data were averaged to daily values and subsequently interpolated

to match the grid resolution of the column concentration fields described in Sect. 2.3.1.

Digital elevation data were obtained from the GMTED2010 dataset (https://www.usgs.gov/coastal-changes-and-impacts/gmted2010, last access: 29 January 2026) (Danielson and Gesch, 2011). The DEM was resampled and mapped to the same spatial grid as the concentration and wind fields to ensure consistency across all datasets.

2.1.4 Emissions Inventory

In this study, multiple emission inventories were used to estimate fossil fuel CO_2 ($ffCO_2$) emissions and to calculate the CO_2-to-NO_x ratio. In the urban observation system simulation experiment (Sect. 3), the GEMS inventory (0.1° resolution) for NO_x and CO_2 emissions (Huang et al., 2017) was used to derive the prior CO_2-to-NO_x ratio (available at: https://gems.sustech.edu.cn/data, last access: 29 January 2026). For comparison, we also employed the gridded fossil fuel CO_2 emissions inventory from the Open-source Data Inventory for Atmospheric Carbon dioxide (ODIAC, Version 2024, 1 km resolution; https://db.cger.nies.go.jp/dataset/ODIAC/, last access: 29 January 2026). In Sect. 4, we further utilized the sectoral and 0.1° gridded NO_x and CO_2 inventories from the Emissions Database for Global Atmospheric Research (EDGAR; https://edgar.jrc.ec.europa.eu/emissions_data_and_maps, last access: 29 January 2026) (Crippa et al., 2018), as well as the sectoral NO_x and CO_2 inventories from the Multi-resolution Emission Inventory model for Climate and air pollution research (MEIC; http://meicmodel.org.cn/, last access: 29 January 2026) (Team, 2012). Using different approaches to calculate the CO_2-to-NO_x ratio, we quantified the variations arising from different inventory inputs and assessed their impact on emission inversions.

2.2 Methodology

2.2.1 Calculation of Prior Distribution for CO_2 Emissions

(1) Mass Balance Method

In previous studies, numerous works have detailed the theoretical derivation for inferring gridded fluxes from column observations (Huang et al., 2024; Koene et al., 2024; Qin et al., 2023; Rey-Pommier et al., 2025; Sun, 2022). Such frameworks are generally based on solutions to the atmospheric continuity equation. Divergence-based approaches typically rely on several key assumptions: (1) exchanges above the planetary boundary layer (column top) and at the surface (column bottom) are neglected, effectively assuming two-dimensional diffusion; (2) horizontal turbulent transport is ignored at coarse grid resolutions; and (3) the deposition term S is treated using a first-order chemical approximation. Starting from the unsteady, source-driven atmospheric continuity equation, the gridded flux of a given species, such as NO_2, can be derived from satellite column observations, with the resulting flux $\langle E_{NO_2} \rangle$ expressed as in Eq. (1).

$$\langle E_{NO_2} \rangle = \langle \boldsymbol{u} \times (\nabla V_{NO_2}) \rangle \frac{\langle V_{NO_2} \boldsymbol{u}_{10} \times (\nabla z_0) \rangle}{H} + \frac{\langle V_{NO_2} \rangle}{\tau} \tag{1}$$

The detailed derivation is provided in Appendix A2. To fully exploit the available data while accounting for observational errors, spatial gradients were computed along the zonal, meridional, and both diagonal directions. Gradients were numerically approximated using second-order central differences, multiplied by the corresponding decomposed wind vectors, and then averaged. For boundary grid points, one-sided differences were applied. Although using gradients in multiple directions helps reduce directional dependence, the finite-difference gradient operator can amplify high-frequency retrieval noise in the original NO_2 column field. Therefore, the divergence-derived NO_x fluxes should not be interpreted as purely deterministic grid-cell emissions. Instead, they represent monthly aggregated estimates subject to retrieval noise, wind-field uncertainty, chemical-parameter uncertainty, and possible structured errors introduced by gradient operations and gridding. We further evaluate this sensitivity in Appendix A5.

(2) Convert NO_2 to NO_x

Nitrogen oxides ($NO_x = NO + NO_2$) do not exist independently in the troposphere, as NO and NO_2 continuously interconvert, while the total NO_x remains relatively stable. To convert between NO_2 column densities and total NO_x columns, Sun et al. (2018a) applied a fixed coefficient of 1.32. In this study, we adopt a more rigorous approach to derive the conversion factor, as expressed in Eq. (2) (Beirle et al., 2023), based on the photostationary steady-state assumption:

$$\begin{cases} V_{NO_x} = \alpha V_{NO_2} = \left(1 + \dfrac{J}{K X_{O_3}}\right) V_{NO_2} \\ J = k_1 \times \exp\left(-\dfrac{k_2}{\cos(\mathrm{SZA})}\right) \\ K = k_3 \times \exp\left(-\dfrac{k_4}{T}\right) \end{cases} \tag{2}$$

here, J represents the photolysis frequency of NO_2, calculated following the methodology in Dickerson et al. (1982). The rate constants k_1 and k_2 are set to 0.0167 and 0.575, respectively. The solar zenith angle (SZA) can be directly determined from the local latitude, longitude, and time; in this study, SZA values are obtained from the TROPOMI satellite metadata. K denotes the chemical reaction rate constants for NO with O_3, expressed in $cm^3\,(mol\,s)^{-1}$ and recommended by IUPAC, with $k_3 = 2.07 \times 10 - 12$ and $k_4 = 1400$. The

ozone mixing ratio, X_{O_3}, is derived from the ESCiMo project (Jöckel et al., 2016), and T represents the boundary-layer mean temperature obtained from ERA5 reanalysis data. Under these definitions, Eq. (2) can be rewritten as:

$$X = \alpha \times \langle E_{NO_2} \rangle \quad (3)$$

Using Eq. (3) we can obtain grid-resolved estimates of NO_x fluxes, which serve as the prior distribution for fossil fuel CO_2 ($ffCO_2$) emissions. These estimates provide a data-driven prior inventory for subsequent steps in the inversion framework.

(3) Scale height and Chemical lifetime

Regarding the selection of scale height and first-order chemical lifetime, previous studies, such as Beirle et al., employed fixed empirical scale height values and adjusted terrain correction terms to obtain optimal estimates (Beirle et al., 2023). Their chemical lifetime was calculated using a compensation method that accounted for losses integrated over residence times within a 15 km buffer. While effective at point-source scales, this approach is not directly applicable to our study. In the present work, we follow Sun et al.'s (2018b) purely data-driven approach, which leverages observational data without introducing additional assumptions, constructing a linear regression model to determine these parameters (Sun, 2022). This observation-driven fitting method not only reduces errors arising from new assumptions but also mitigates biases caused by grid resampling and near-surface wind selection.

To suppress excessive noise in single-day fits, we perform monthly regressions and adopt the temporal and spatial mean over the month as the final estimate, representing an aggregate over the full spatial domain, the entire month, and the troposphere. The retrieved scale height and first-order chemical lifetime are then applied back into Eqs. (4) and (6) to obtain the final gridded NO_x vertical fluxes.

After terrain correction, the gridded flux fields remove a substantial portion of strong emission signals obscured by wind divergence and negative divergence artifacts, while the chemical correction term adjusts residual minor negative biases (Sun, 2022; Beirle et al., 2023). Any remaining small negative values after these corrections are set to zero.

(4) Calculation of Prior CO_2-to-NO_x Ratio

We used the prior CO_2-to-NO_x ratio in combination with TROPOMI-derived NO_x emission distributions to obtain an initial characterization of urban prior $ffCO_2$ emissions. Following the approach of Feng et al. (2024), who calculated the CO_2-to-NO_x ratio by dividing gridded CO_2 and NO_x emission inventories, we derived city-specific prior CO_2-to-NO_x ratio using the 0.1° CO_2 and NO_x inventories from GEMS (https://gems.sustech.edu.cn/data/database, last access: 29 January 2026). Unlike Feng et al. (2024), who focused on grid-level CO_2-to-NO_x ratio, we fitted the gridded ratios across each study region to obtain an integrated city-level CO_2-to-NO_x ratio, which is more suitable for subsequent inversion analyses (Fig. 3). Details on the associated uncertainties are provided in Sect. 4.1.

Figure 3 illustrates our method for calculating the prior CO_2-to-NO_x ratio. By fitting the 0.1° gridded ratios for each city, we obtained overall city-scale values. The coefficients of determination (R^2) for Paris, Cairo, and Beijing were 0.96, 0.917, and 0.76, respectively.

Recently, an increasing number of studies have employed NO_x emissions to estimate $ffCO_2$ emissions (Feng et al., 2024; Zheng et al., 2020; Xu et al., 2025b; Yang et al., 2023; Zhang et al., 2022). In inversion methods based on NO_x emissions, the choice of the prior CO_2-to-NO_x ratio directly affects the emission estimates. Uncertainty in the prior ratio propagates to the estimated $ffCO_2$ emissions, influencing both their magnitude and spatial distribution. To evaluate this effect, we selected several widely used CO_2-to-NO_x ratio calculation methods and systematically assessed their associated uncertainties (results see Sect. 4.1 and Appendix A6).

- M.1 Grid-level CO_2-to-NO_x ratio derived directly from gridded CO_2 and NO_x inventories (Feng et al., 2024). Since this study scales emissions to the city level, we further fitted the grid-level ratios to obtain city-integrated CO_2-to-NO_x ratios. M.1 calculations were based on the GEMS gridded inventory.

- M.2 CO_2-to-NO_x ratios calculated using sectoral emission factors for CO_2 and NO_x(Zheng et al., 2020). We derived city-scale ratios by aggregating across all sectors. M.2 used the GEMS sectoral emission factors.

- M.3 CO_2-to-NO_x ratios derived from near-real-time satellite observations. Background-stable NO_x plumes were used to constrain CO_2 plumes, and joint fitting of the two concentrations was performed using the cross-sectional flux method (Xu et al., 2025b; Reuter et al., 2019). The CO_2-to-NO_x ratio was obtained directly from the half-width at half-maximum. Following this approach, we used TROPOMI and OCO-2 observations to calculate city-scale ratios.

- M.4 Same as M.2, but the MEIC sectoral inventory was used for Beijing.

- M.5 Same as M.1, but calculations were based on the EDGAR gridded inventory.

- M.6 Same as M.2, but calculations were based on the EDGAR sectoral inventory.

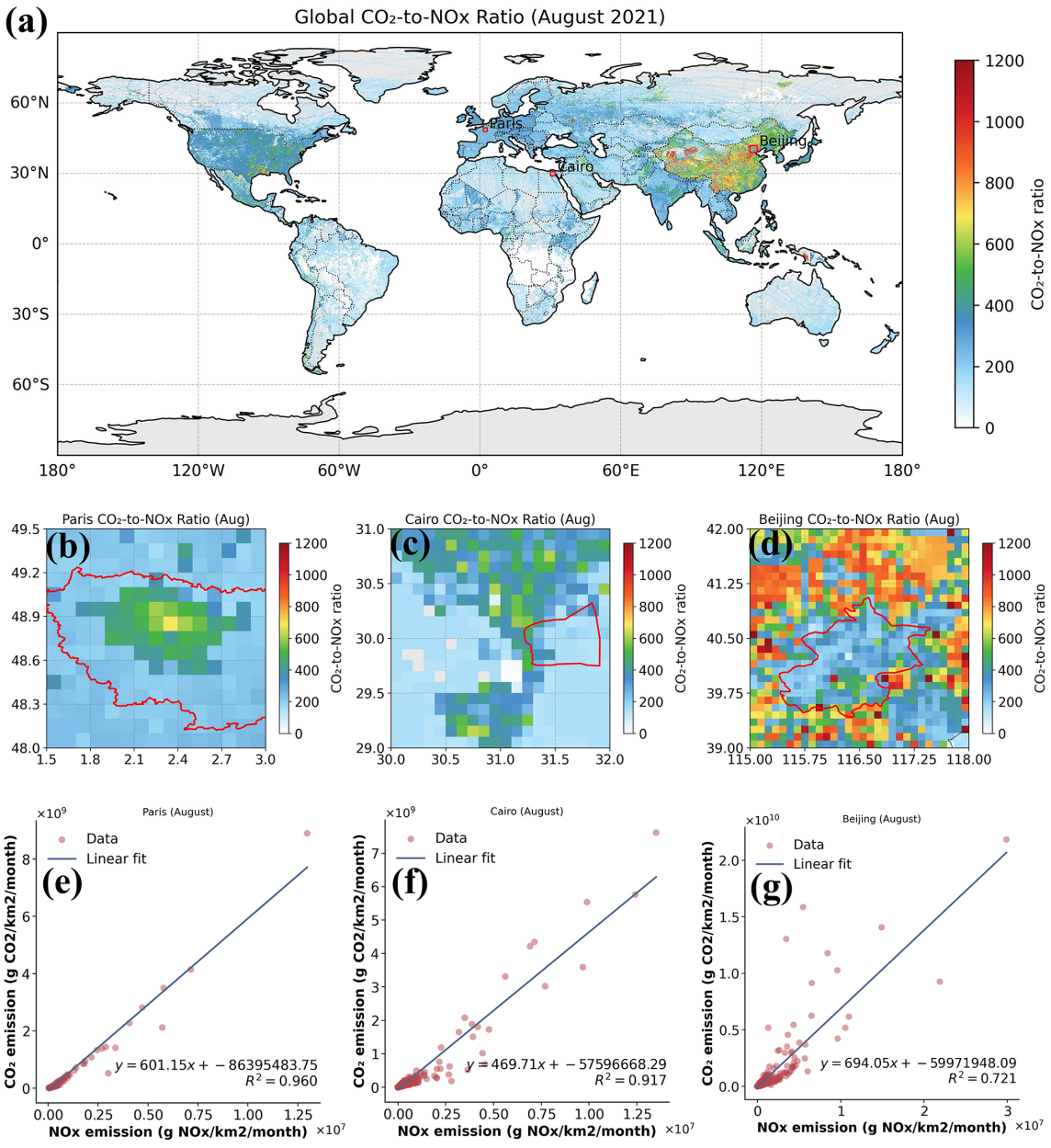

Figure 3. Schematic diagram of prior CO_2-to-NO_x ratio calculation methods. Panel **(a)** shows the global gridded CO_2-to-NO_x ratio derived from GMES data. Panels **(b)–(d)** present the gridded CO_2-to-NO_x ratio for Paris, Cairo, and Beijing (the red lines indicate the boundaries of each city). Panels **(e)–(g)** display the overall CO_2-to-NO_x ratio fitting results for the three cities. We used the Île-de-France administrative boundary to depict Paris in the figures, rather than the city proper. Although our actual study area only covers a subset of Île-de-France (1.5–3° E, 48–49.5° N)

2.2.2 Estimating ffCO_2 emissions by WRF-STILT simulations

(1) Quantifying ffXCO_2 enhancements

Distinguishing anthropogenic emission signals from the surrounding "clean" background in XCO_2 observations is a central challenge for constraining urban carbon emissions via satellite. Definitions of "background" vary across studies. In this work, we define the background as atmospheric XCO_2 that is unaffected by local emissions within the study region. Following the approach proposed by Ye et al. (2020) in constraining urban emissions using OCO-2 observations, we adopt a baseline calculation strategy that incorporates latitudinal gradients.

In this framework, XCO_2 is decomposed into two components: $XCO_{2\text{trend}}$, representing the regional-scale, non-local

trend, and $XCO_{2\text{local}}$, whose standard deviation σ_{local} characterizes local-scale variability. Samples satisfying $XCO_2 < XCO_{2\text{trend}} + 0.5\sigma_{\text{local}}$ are selected as "background samples," as they exhibit lower local spatial variability compared with data influenced by fossil fuel emissions. These background samples are then subjected to linear regression to derive the background baseline and characterize its spatial variation.

(2) X-Stochastic Time-Inverted Lagrangian Transport model for ACDL productions

We employ the X-STILT V1 model to trace CO_2 concentration variations driven by prior emission information. X-STILT integrates satellite profile data and enables a comprehensive uncertainty assessment of urban XCO_2 enhancements on a per-observation basis (Wu et al., 2018). Originally developed to extract urban signals from passive OCO-2 XCO_2 observations, we have adapted the framework for use with the active CO_2 satellite DQ-1, with appropriate modifications. The relationship between XCO_2^{Lidar} (DQ-1 XCO_2 observations) measurements and the CO_2 vertical profile, CO_2(p), can be formulated as follows:

$$\begin{aligned} XCO_2^{\text{Lidar}} &= \frac{\int_{\text{p\_surface}}^{\text{p\_toa}} CO_2(p)\text{WF(p)}}{\int_{\text{p\_surface}}^{\text{p\_toa}} \text{WF(p)}\,\mathrm{d}p} \\ &= \sum_{n=1}^{\text{toa}} \frac{\text{WF}(p_n)}{\text{IWF}} \times CO_2(p_n) \end{aligned} \tag{4}$$

here, p_toa represents the pressure at the bottom height of the ACDL, and p_surface represents the pressure corresponding to the surface elevation at the laser footprint. WF and IWF denote the weighting function and the normalized weighting function of the ACDL, respectively. A detailed description is provided in Appendix A1.

We approximate the CO_2 concentration by summing the background concentration with the simulated ffCO_2 enhancement. Here, the simulated ffCO_2 enhancement, $\Delta CO_{2\text{ff}CO_2}(p) = \langle \text{ff}CO_2, \text{foot}(p)\rangle$, is obtained by interpolating the modeled ffCO_2 fluxes along tracer-tagged footprints. Consequently, the relationship between the ffCO_2 fluxes and the simulated $XCO_2^{\text{Lidar}}_{\text{mod}}$, is established, yielding the modeled fossil fuel CO_2 enhancement $XCO_2^{\text{Lidar}}_{\text{ff}CO_2,\text{mod}}$ along the lidar track:

$$\begin{aligned} XCO_2^{\text{Lidar}}_{\text{ff}CO_2,\text{mod}} &= XCO_2^{\text{Lidar}}_{\text{mod}} - XCO_2^{\text{Lidar}}_{\text{background}} \\ &= \sum_{n=1}^{\text{toa}} \frac{\text{WF}(p_n)}{\text{IWF}} \times \langle \text{emissions}, \text{foot}(p_n)\rangle \end{aligned} \tag{5}$$

$XCO_2^{\text{Lidar}}_{\text{background}}$ represents the background concentration along the selected DQ-1 orbit (see Sect. 2.2.2 (1)). The operator $\langle,\rangle$ denotes an inner product, emissions is the prior emission flux, and foot(p_n) represents the modeled footprint at different vertical layers. Using the above formulation, the mathematical foundation for the inversion is established. By integrating footprints across multiple release heights, the equation can be further simplified. In this study, we define the ffXCO_2 enhancement simulated via the atmospheric transport model as:

$$\text{XSTILT}^{\text{Lidar}} = \sum_{n=1}^{\text{toa}} \frac{\text{WF}(p_n)}{\text{IWF}} \times \text{foot}(h_n) \tag{6}$$

$$XCO_2^{\text{Lidar}}_{\text{ff}CO_2,\text{mod}} = \langle \text{XSTILT}^{\text{Lidar}}, \text{emissions}\rangle \tag{7}$$

here, $\text{XSTILT}^{\text{Lidar}}$ is defined as the column-averaged footprint, corresponding to the column-averaged CO_2 concentration. The inner product of the column-averaged footprint and the prior emission flux yields the simulated XCO_2 enhancement.

(3) Bayes inversion

We used the NO_x emissions obtained previously as prior fluxes and, through the CO_2-to-NO_x ratio, established the relationship between the prior emissions and the XCO_2 observed by DQ-1 (Eq. 9). The XCO_2 enhancements estimated from DQ-1 observations were then employed to impose "top-down" constraints on the simulated results. Following the approaches of Che et al. (2024); Ye et al. (2020); Sheng et al. (2025), we applied a Bayesian inversion framework to optimize the prior emission estimates.

$$y_{\text{obs}} = y_{\text{sim}} \times \lambda + \varepsilon_{\text{p}} \tag{8}$$

here, y_{obs} and y_{sim} represent the observed ffXCO_2 enhancements and the simulated NO_x enhancements, respectively. The symbol λ denotes the CO_2-to-NO_x ratio, and ε_{p} represents the observational error, which encompasses contributions from DQ-1 measurement uncertainties, model errors, and errors in model parameters. It is defined as follows:

$$\begin{cases} y_{\text{obs}} = \int_{\text{latitude1}}^{\text{latitude2}} \text{ff}XCO_{2\text{obs}}\,\mathrm{d}t \\ y_{\text{sim}} = \int_{\text{latitude1}}^{\text{latitude2}} \langle X, \text{footprint}\rangle\,\mathrm{d}t \end{cases} \tag{9}$$

$$\varepsilon_{\text{obs}} = \sqrt{\sigma^2_{\text{measurement}} + \sigma^2_{\text{sim}}} \tag{10}$$

In this context, ff$XCO_{2\text{obs}}$ represents the DQ-1 XCO_2 enhancement after background concentration removal. The notation ⟨Xfootprint⟩ denotes the simulated NO_x enhancement, obtained by convolving the NO_x emission inventory X with the STILT-derived footprint (It should be noted that the footprints used here represent hourly footprints during the simulation period, whereas the NO_x emissions are monthly emissions derived using the method described in Sect. 2.2.1. Therefore, we use the New High Resolution Temporal Profiles in EDGAR dataset (https://edgar.jrc.ec.europa.eu/dataset_temp_profile, last access: 29 January 2026) to distribute the monthly NO_x emissions to each hourly footprint). Pseudo-observations, ff$XCO_{2\text{obs}}$, are generated by averaging DQ-1 measurements over one-second intervals along the satellite track (∼ 7 km), together with the corresponding simulated values.

Following the Bayesian inversion approach, the state vector λ is expressed in terms of the CO_2-to-NO_x ratio, representing the relationship between urban fossil fuel CO_2 and NO_x emissions. The Jacobian matrix is derived from the simulated NO_x enhancement y_{sim}. Here, $\sigma^2_{measurement}$ represents the observational error variance, and σ^2_{sim} denotes the model transport error variance. DQ-1 observations are assumed unbiased with respect to the true state. To account for measurement uncertainty, random Gaussian noise with a standard deviation of 0.3 ppm – representing the lower limit of observational error – is added to the observations.

By minimizing the loss function, we obtain the posterior CO_2-to-NO_x ratio $\hat{\lambda}$ and posterior uncertainty $\hat{\sigma}$:

$$\hat{\lambda} = \lambda + \sigma^2_{sim} y^T_{sim} \left(y_{sim} S_{obs} y^T_{sim} + S_{obs}\right)^{-1} \times (y_{obs} - y_{sim}\lambda) \quad (11)$$

$$\hat{\sigma}^2 = \left(y^T_{sim} S^{-1}_{obs} y_{sim} + \sigma^{-2}_{sim}\right)^{-1} \quad (12)$$

here, S_{obs} is a diagonal matrix, with the diagonal entries representing the observational error variances ε^2_{obs} for each orbit. The prior uncertainty σ_{sim} is primarily derived from the uncertainties in the prior NO_x emission distribution σ_{NO_x} and the prior CO_2-to-NO_x ratio $\sigma_{C/N}$ as Eq. (13):

$$\sigma_{sim} = \sqrt{\sigma^2_{NO_x} + \sigma^2_{C/N}} \quad (13)$$

3 Urban Observation System Simulation Experiment

3.1 Satellite-driven urban NO_x emission distribution

As described in Sect. 2.2.1, we applied the mass balance approach in the three cities to derive prior NO_x gridded inventories, which serve as the basis for constructing $ffCO_2$ gridded emissions. The grid resolution was set to 5 km × 5 km. Figure 4 illustrates the detailed NO_x fluxes for August 2022 over Beijing, Paris, and Cairo, produced entirely via a top-down approach, with panels (a)–(c) corresponding to Beijing, Paris, and Cairo, respectively.

From the figure, it is evident that the average NO_x flux magnitude in all three cities is on the order of $\sim 10^{-8}$ mol m^{-2} s^{-1}. However, their spatial distributions differ considerably. Both Paris and Cairo exhibit highly concentrated emission patterns. In Cairo, the central urban area and industrial zones display peak NO_x fluxes on the order of $\sim 10^{-7}$ mol m^{-2} s^{-1}. These high-flux regions sharply decrease with distance from the center, highlighting a pronounced urban boundary effect (Li et al., 2025). In contrast, Beijing not only exhibits strong emissions in the central urban area (within the Sixth Ring Road) but also features numerous dispersed point- and area-like sources in suburban districts (e.g., Fangshan in the southwest) and in the surrounding hills and mountains. Compared with Cairo's concentrated emissions, Beijing's peak NO_x grid flux in the urban core is nearly one order of magnitude lower (see the color scale mapping in Fig. 4); however, due to the city's larger spatial extent, the total flux remains substantially higher than that of Cairo.

Beijing's topography, with higher elevations in the northwest and lower elevations in the southeast, can induce local wind divergence over hilly and mountainous areas. This effect may generate false positives when using the divergence method (Sun et al., 2021; Liu et al., 2021). In the northwestern suburban mountains of Beijing, the mean wind divergence can reach magnitudes of $\sim \pm 10^{-4}$ s^{-1}, while TROPOMI NO_2 column densities are on the order of 10^{-4} mol m^{-2}. Such magnitudes are comparable to mid-scale urban averages or point-source emissions. Neglecting the divergence term can result in genuine emissions being omitted, while background fluxes induced by terrain or wind divergence are mistakenly included. Following Sun (2022), we applied Eq. (A5) to reconstruct the wind-divergence term using surface wind and terrain gradients, thereby reintegrating previously neglected area-like emissions. Using Beirle et al.'s methodology, we integrated the net gridded fluxes within a 60 km radius centered on Beijing over the entire year of 2022 to estimate the city's annual NO_x emissions at 251 450 t. This value is approximately 9.7 % higher than the 2022 annual emission reported in the MEIC inventory for Beijing (227 000 t). Although the total magnitude is consistent, the spatial distribution from top-down estimates differs substantially from bottom-up inventories. Section 3.2.2 further analyzes these differences by simulating urban $ffCO_2$ plumes using both our $ffCO_2$ inventory and the ODIAC inventory.

By comparison, Paris and Cairo are situated on relatively flat terrain (maximum elevation $\sim$ 180 m). Terrain-induced wind divergence is negligible relative to total fluxes (wind-terrain and divergence contributions $\sim 10^{-10}$ mol m^{-2} s^{-1}), leaving the continuity equation primarily governed by wind-weighted column gradients. Cairo, located upstream of the Nile Delta in a high-albedo desert region, benefits from low uncertainty in satellite-derived NO_2 columns. Under these conditions, the top-down NO_x inventory closely aligns with the bottom-up inventory in terms of spatial distribution. Paris, situated in the Paris Basin along the Seine River, experiences minimal terrain gradients. Although less extreme than Cairo, the slight topographic variation still produces pronounced urban boundary effects in the inversion results.

To quantitatively compare the NO_x emission characteristics and atmospheric behavior among Beijing, Paris, and Cairo, derived using the mass balance approach, we analyzed key parameters for August, including mean NO_x fluxes, total emissions, chemical lifetimes, vertical distribution scale heights, and NO_x/NO_2 ratios (Table 1). These NO_x behavior parameters reflect heterogeneous characteristics shaped by the interplay of emission intensity, photochemical conditions, and boundary layer structure.

In terms of mean NO_x flux per unit area (mol m^{-2} s^{-1}), Cairo exhibits the highest value (0.35×10^{-8}), followed by

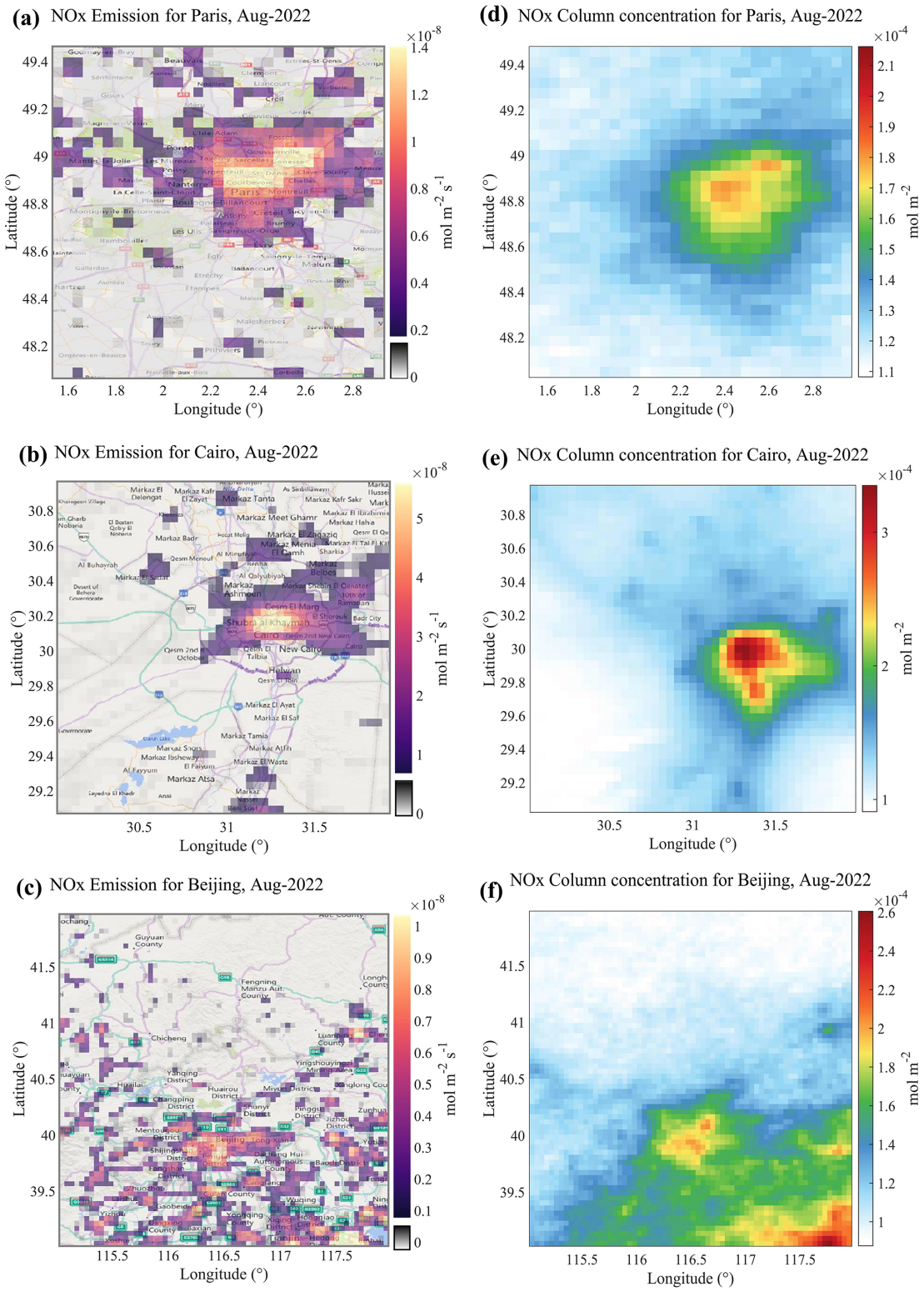

Figure 4. Gridded prior NO_x emission inventories derived from the mass balance method. Panels **(a)–c)** show the NO_x flux distributions (unit: mol m^{-2} s^{-1}) for Beijing, Paris, and Cairo in August 2022. Panels **(d)–f)** present the resampled monthly mean NO_2 column concentration distributions for the three cities. Basemap for panels **(a)–(c)**: Esri World Topographic Map. Sources: Esri, HERE, Garmin, Intermap, INCREMENT P, GEBCO, USGS, FAO, NPS, NRCan, GeoBase, IGN, Kadaster NL, Ordnance Survey, Esri Japan, METI, Mapwithyou, NOSTRA, ©OpenStreetMap contributors, and the GIS user community | Powered by Esri.

Paris (0.28×10^{-8}) and Beijing (0.24×10^{-8}), indicating a higher emission of urban emission sources in Cairo – particularly from traffic – resulting in stronger NO_x release per unit surface area. Nevertheless, Beijing's total NO_x emissions (182 800 t yr^{-1}) are substantially higher than those of the other two cities, reflecting its larger urban extent and greater overall emission intensity, characteristic of a complex multi-source emission profile.

The first-order chemical lifetime of NO_x in the atmosphere indicates its removal rate and is influenced by factors such as OH radical concentration and solar radiation intensity. Paris exhibits the longest NO_x chemical lifetime (6.91 h), followed by Beijing (4.70 h) and Cairo (2.93 h). These differences are closely linked to photochemical activity: strong summer sunlight and high temperatures in Cairo enhance OH-driven removal reactions, whereas the relatively mild mid-latitude climate of Paris, combined with emission control measures, prolongs NO_x lifetime.

Regarding vertical distribution, the NO_x scale height also varies across the three cities. Beijing shows the highest scale height (2.08 km), reflecting the combined effects of strong convective transport and multi-source emissions that elevate NO_x into the upper mixing layer. By contrast, Cairo (1.41 km) and Paris (1.21 km) display more typical boundary-layer-constrained distributions, indicating that ground-level emission controls and thermal structure strongly modulate vertical NO_x transport.

Finally, the NO_x/NO_2 ratio provides insight into the proportion of NO and its degree of conversion. Beijing exhibits the highest ratio (1.41), followed by Cairo (1.32) and Paris (1.29), suggesting a higher fraction of NO in Beijing, likely associated with dense traffic sources and a larger fraction of primary NO emissions. The relatively lower ratio in Paris reflects a higher NO_2 fraction, consistent with effective emission controls and extensive photochemical conversion.

3.2 Urban Fossil Fuel XCO_2 Enhancement (ffXCO_2)

In this section, we summarize the prior ffXCO_2 emissions for each study region. For the selected orbits, the total monthly emissions of Beijing, Paris, and Cairo were approximately 7.47–9.94, 2.91–3.33, and 2.73–3.60 Mt C per month, respectively. To constrain emissions, we compared observed and simulated ffXCO_2 enhancements, where ffXCO_2 enhancement is defined as the increase in XCO_2 relative to the background level caused by local fossil fuel emissions. The prior ffXCO_2 enhancements were simulated by taking the inner product of prior NO_x emissions inventories with STILT footprints, while the observed enhancements from DQ-1 were derived by subtracting the background concentration from the measured XCO_2. By comparing prior and observed ffXCO_2 enhancements, we assessed the variability of ffXCO_2 along the orbit and investigated the sources and detectability of the ffXCO_2 signal.

3.2.1 Comparison of Modeled and Observed ffXCO_2

Complex horizontal wind fields can lead to elongated and non-Gaussian plume structures in simulated ffXCO_2 distributions (Ye et al., 2020). This feature is illustrated in Fig. 5c–f. Figure 5a and b show the simulated and observed XCO_2 along two overpasses (simulated XCO_2 is obtained by adding the simulated ffXCO_2 to the background derived in Sect. 2.2.2 (1)). Along these overpasses, ffXCO_2 enhancements exceeding 5 and 10 ppm were observed, with the measured enhancements consistently larger than the simulated values. Although the simulated peak on 7 August is narrower than the observed peak, and the observed peak near 48.4° on 21 August shows a $\sim 0.3°$ displacement relative to the simulation, the overall magnitude of simulated ffXCO_2 agrees well with observations.

To further evaluate the feasibility of constraining fossil fuel CO_2 emissions using the NO_x inventory, we performed a comparative analysis using the ODIAC inventory. We compared simulated ffXCO_2 during the satellite overpasses based on the NO_x and ODIAC inventories (colored shaded areas in the figure), as well as their contributions to the pseudo-observed XCO_2 at the satellite locations (colored dots), where the red line represents enhancements derived from the NO_x inventory and the green line represents those from ODIAC. Over Paris, the NO_x-based simulation yields higher ffXCO_2 enhancements than ODIAC, likely due to uncertainty in the prior CO_2-to-NO_x ratio. Nonetheless, both inventories capture enhancements exceeding 4 ppm. Moreover, the line plots indicate that the temporal variation and magnitude of the simulated concentration contributions (red and green lines) are nearly identical.

We examined local ffXCO_2 enhancements during two overpasses of Cairo on 2 August 2022 at 11:00 and 19 August 2022 at 23:00 LT. As shown in Fig. 6, the simulated ffXCO_2 peaks exceed 6 ppm. In contrast to Paris, where enhancements are widespread, diffuse, and lack clear structure, and Beijing, where plumes exhibit complex patterns, the simulated ffXCO_2 over Cairo is strongly influenced by northwesterly winds, resulting in well-defined plumes. Figure 5a illustrates that the simulations based on both inventories on 2 August produce similar magnitudes and trends, consistent with the Paris results, where the NO_x-based simulation exceeds that from ODIAC. Notably, the simulated peaks on 2 August also show a spatial offset relative to the observations. Following Ye et al., 2020, such offsets are attributed to the satellite trajectory crossing the plume edges nearly parallel to the plume axis, making the simulated ffXCO_2 highly sensitive to errors in the horizontal wind field.

Notably, the overpasses above Paris and Cairo (Figs. 5a and 6b) exhibit higher latitudinal gradients in the background XCO_2, as indicated by the background lines. The approach used to derive these background lines provides a reliable estimate of background XCO_2 because, within the relevant regions, the observed and modeled cumulative ffXCO_2 en-

Table 1. Grid-averaged NO_x fluxes, with total urban NO_x emissions as intermediate parameters in the mass balance method.

City	NO_x average flux ($mol\,(m^2\,s)^{-1}$)	NO_x total emission (kt per month)	Chemical lifetime (h)	Scale height (km)	NO_x/NO_2
Beijing	0.23510^{-8}	15.29	4.69	2.07	1.41
Paris	0.27710^{-8}	4.45	6.90	1.21	1.29
Cairo	0.35310^{-8}	6.78	2.93	1.40	1.32

Details of the uncertainties are provided in the Appendix A5.

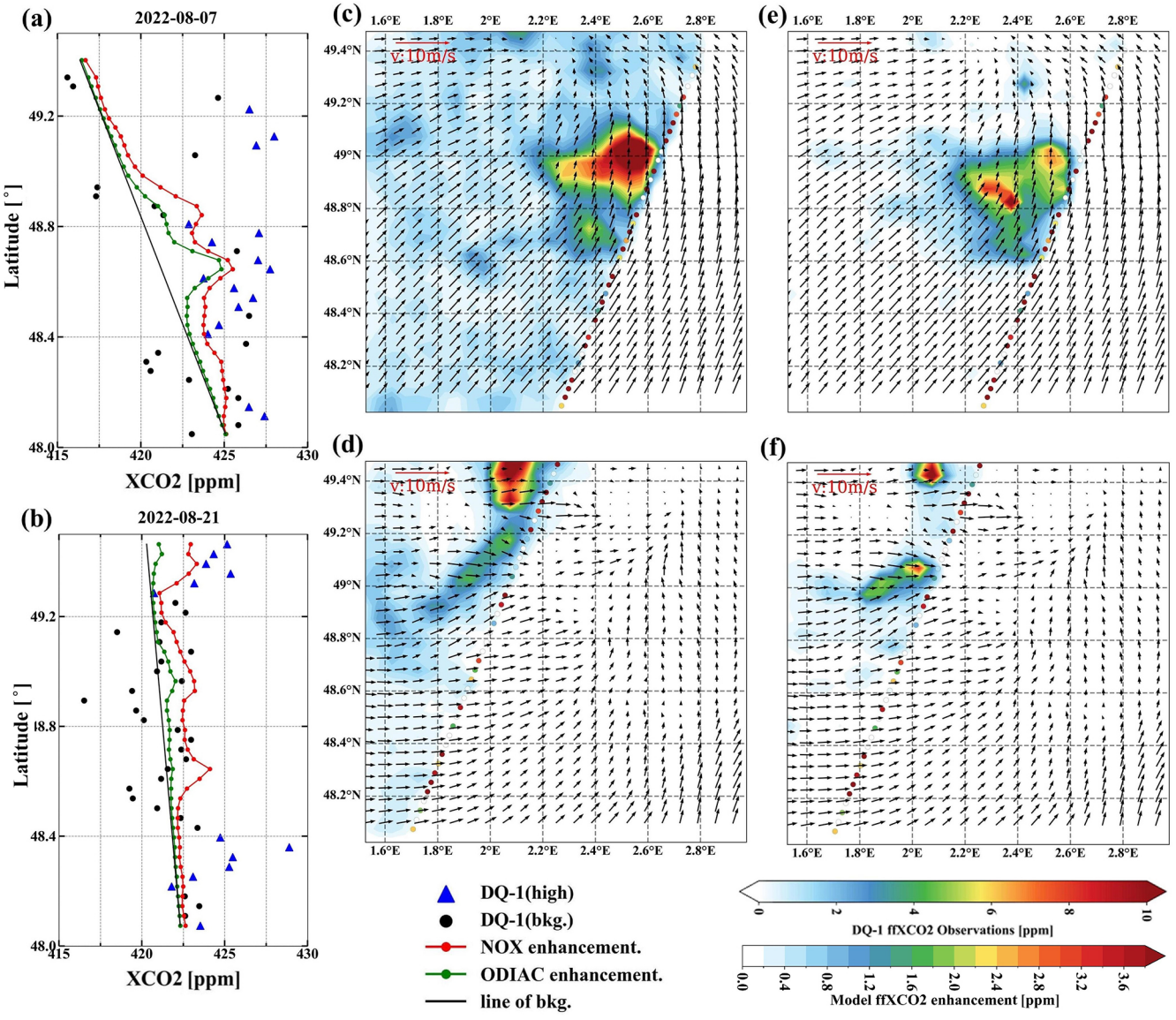

Figure 5. Comparison between simulated and observed ffXCO_2 enhancements using DQ-1 overpasses above Paris on 7 and 21 August 2022 at 01:00 UTC. Panels **(a)**, **(b)** show DQ-1 XCO_2 along the two tracks (black dots and blue triangles) and simulated XCO_2 (red solid line: sum of background concentration and ffXCO_2 simulated using the NO_x emissions; green solid line: sum of background concentration and ffXCO_2 simulated using the ODIAC inventory), averaged over 0.5 s. Black circles denote the data used to derive the background concentration (black solid line). Panels **(c)–f)** show simulated ffXCO_2 and observed ffXCO_2 retrieved from DQ-1 data ((**c, d**): based on the NO_x inventory; **(e, f)**: based on the ODIAC inventory). Background XCO_2 concentrations have been subtracted. The reference vector indicates a wind speed of $10\,m\,s^{-1}$.

hancements along the satellite track are largely consistent. Consequently, these findings highlight the effectiveness of the background line method for inferring satellite-observed background XCO_2. They also emphasize that the spatial scale of satellite data analysis is closely linked to the constraints imposed by local emission sources. Neglecting the latitudinal gradient of background XCO_2 may introduce biases in the estimation of ffXCO_2 and, consequently, in derived emission fluxes (Ye et al., 2020).

3.2.2 Comparison of NO_x and ODIAC Modeled ffXCO_2 in Beijing

Figure 7 illustrates the investigation of local ffXCO_2 enhancements over Beijing using two DQ-1 overpasses and corresponding simulated ffXCO_2. In the figure, the colored shading represents XCO_2 concentrations accumulated over the previous 24 h simulated by STILT, while the colored dots indicate satellite-observed XCO_2 enhancements, calculated by subtracting the background values (see Sect. 2.2.2). The red contours outline the urban area of Beijing. As shown, ffXCO_2 over this region can reach approximately 6.0 ppm.

Notably, simulations based on the NO_x inventory (Fig. 7c and d) show that the spatial distribution of ffXCO_2 enhancements varies significantly with meteorological conditions and emission patterns. In contrast, for Paris and Cairo, the simulated ffXCO_2 is more concentrated. Over Beijing, however, the ffXCO_2 distribution is more dispersed and comprises multiple plumes. When comparing simulations using NO_x and ODIAC inventories for Paris and Cairo, the overall plume structures remain largely unaffected. Over Beijing, the simulations using the ODIAC inventory (Fig. 7e and f) display an almost identical ffXCO_2 enhancement distribution across different wind conditions, showing pronounced anomalies in the urban area. Such similarity is unrealistic.

We attribute this behavior to the ODIAC inventory allocating disproportionately high fossil fuel emissions to central Beijing. When STILT footprints intersect the urban area, the high emission gradients in ODIAC (central urban emissions far exceeding suburban values) amplify ffXCO_2 enhancements in the inner city. ODIAC's low-emission thresholds are influenced by nighttime light saturation, with median differences ranging from 47 %–84 %. Consequently, ODIAC artificially concentrates emissions in the city center while underrepresenting surrounding suburban areas. This makes it challenging to accurately constrain CO_2 fluxes in the peripheral regions using ODIAC. Observations from the TCCON Xianghe site further highlight the limitations of ODIAC's emission allocation in the Beijing area.

Figure 8 presents the comparison of August ffXCO_2 at the TCCON site with simulations using the ODIAC and NO_x inventories. Unlike the ffXCO_2 calculation described in Sect. 2.2.2, the TCCON observations provide daily-averaged fossil fuel CO_2 enhancements, where TCCON ffXCO_2 is calculated as TCCON XCO_2 minus background XCO_2 and NEE contributions (details in the Appendix A3). In Fig. 8a, the dark blue line represents ffXCO_2 simulated at the TCCON site using the NO_x inventory, the green line shows the ffXCO_2 simulated after optimization with the inversion using DQ-1 observations, the light blue line corresponds to ODIAC-based simulations, and the red line depicts TCCON-observed ffXCO_2.

Figure 8b quantifies the accuracy of the simulations by plotting the difference between the simulated ffXCO_2 and TCCON observations on the same day and summarizing the monthly mean and standard deviation. The monthly mean absolute difference for the NO_x inventory is 0.82 ppm, while ODIAC exhibits a much larger discrepancy of 5.19 ppm. The inversion-constrained NO_x inventory reduces the mean absolute difference to 0.52 ppm, closely matching TCCON observations. Figure 8c shows the cumulative probability distribution of the differences between simulated and observed ffXCO_2. The differences for the NO_x and inversion-constrained NO_x simulations are largely centered around zero (blue and red lines), whereas for ODIAC, approximately 30 % of differences exceed 5 ppm.

These results indicate that for Beijing in August, simulations based on the NO_x inventory outperform those using ODIAC. Given that the prior ffCO_2 emissions in both inventories are of similar magnitude, the observed discrepancies are primarily attributable to the spatial allocation of emissions in ODIAC. The combined inversion using TROPOMI and ACDL data provides a more accurate reconstruction of urban ffXCO_2 plume structures.

3.2.3 ffCO_2 Inversion Results

This section presents the inversion results of urban carbon emissions for Cairo, Paris, and Beijing, based on TROPOMI and DQ-1 satellite overpass observations (see Table 2). In the inversion, we systematically accounted for observational errors and uncertainties in atmospheric transport to improve the reliability of the emission estimates. From the posterior results, we derived city-specific CO_2-to-NO_x ratios and, by combining them with TROPOMI-derived NO_x emissions, further quantified fossil fuel CO_2 (ffCO_2) emissions. This approach not only enables quantitative assessment of emissions but also provides a scientific basis for cross-city comparisons of emission characteristics, while demonstrating the potential of multi-satellite data for urban emission monitoring.

For the selected orbits, the posterior CO_2-to-NO_x ratios were 428–512 for Cairo, 731–742 for Paris, and 553–640 for Beijing (Table 2). These ratios exhibited clear temporal variability under different background conditions. The magnitude of emissions captured by each orbit depended strongly on its distance from major emission regions and the contemporaneous domain-averaged wind conditions (Che et al., 2022). The domain-averaged wind speeds for the study month (Fig. 9), as well as the high-resolution wind fields at overpass time (black arrows in Figs. 5–7), were consis-

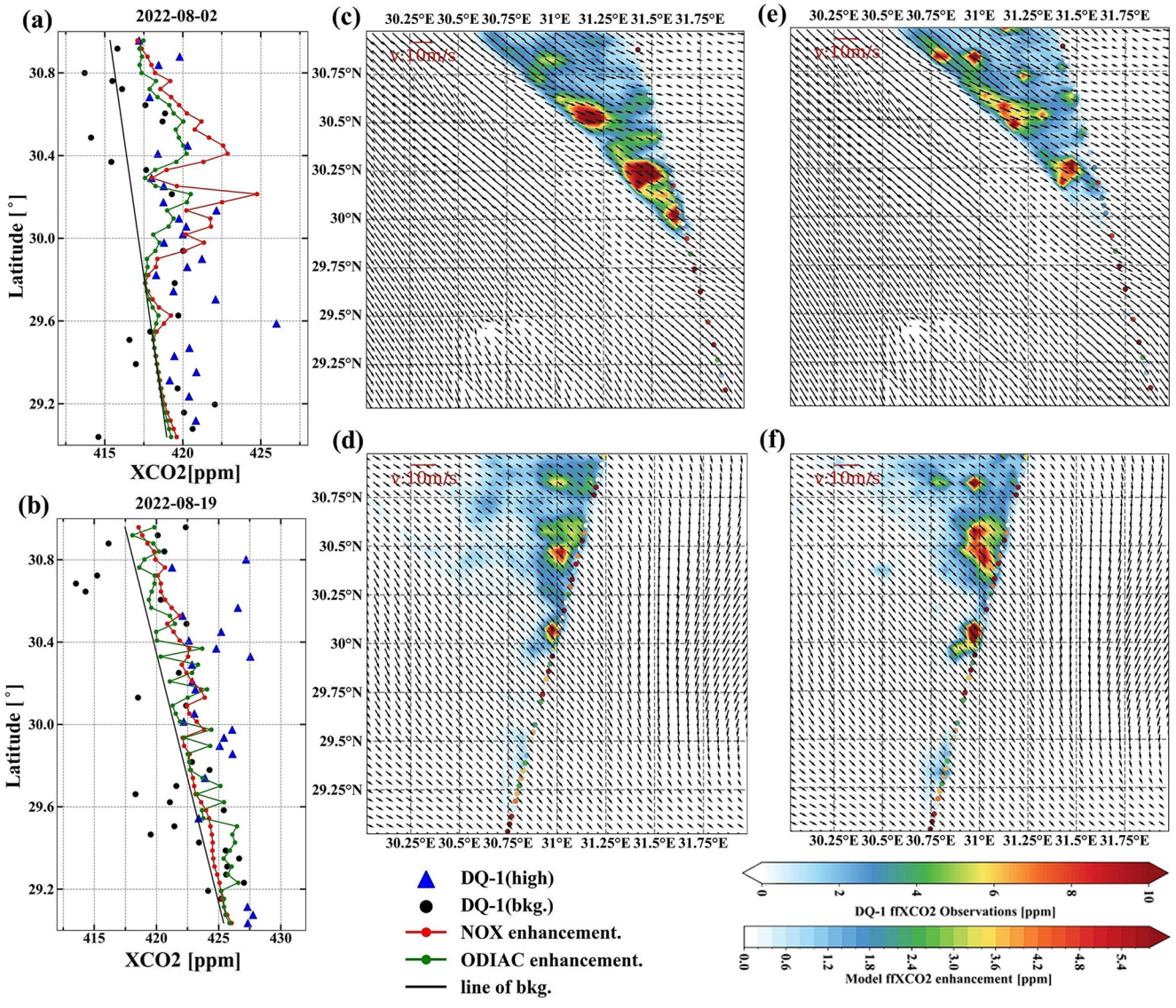

Figure 6. Similar to Fig. 5, comparison between simulated and observed ffXCO_2 enhancements using DQ-1 overpasses above Cairo on 2 August 2022 at 11:00 UTC **(a, c, e)** and 19 August 2022 at 23:00 UTC **(b, d, f)**. Panels **(c)**, **(d)** show the simulated ffXCO_2 enhancements based on the NO_x emissions, while panels **(e)**, **(f)** show those based on the ODIAC inventory.

Table 2. Results of inversion of for CO_2-to-NO_x ratio selected cities using DQ-1 XCO_2 data.

City	Overpass	Prior CO_2-to-NO_x ratio (λ)	Prior uncertainty (%)	Observation uncertainty (ppm)	Model transport uncertainty (ppm)	Posterior CO_2-to-NO_x ratio (λ) and uncertainty
Cairo	2 August 2022	470	40.59 %	1.23	1.75	428 ± 64.58
	19 August 2022			1.06	2.10	512 ± 96.56
Paris	7 August 2022	601	30.12 %	2.45	0.36	731 ± 107.60
	21 August 2022			1.68	0.76	742 ± 138.53
Beijing	9 August 2022	694	28.12 %	2.31	1.28	640 ± 90.11
	16 August 2022			1.79	3.25	553 ± 89.80

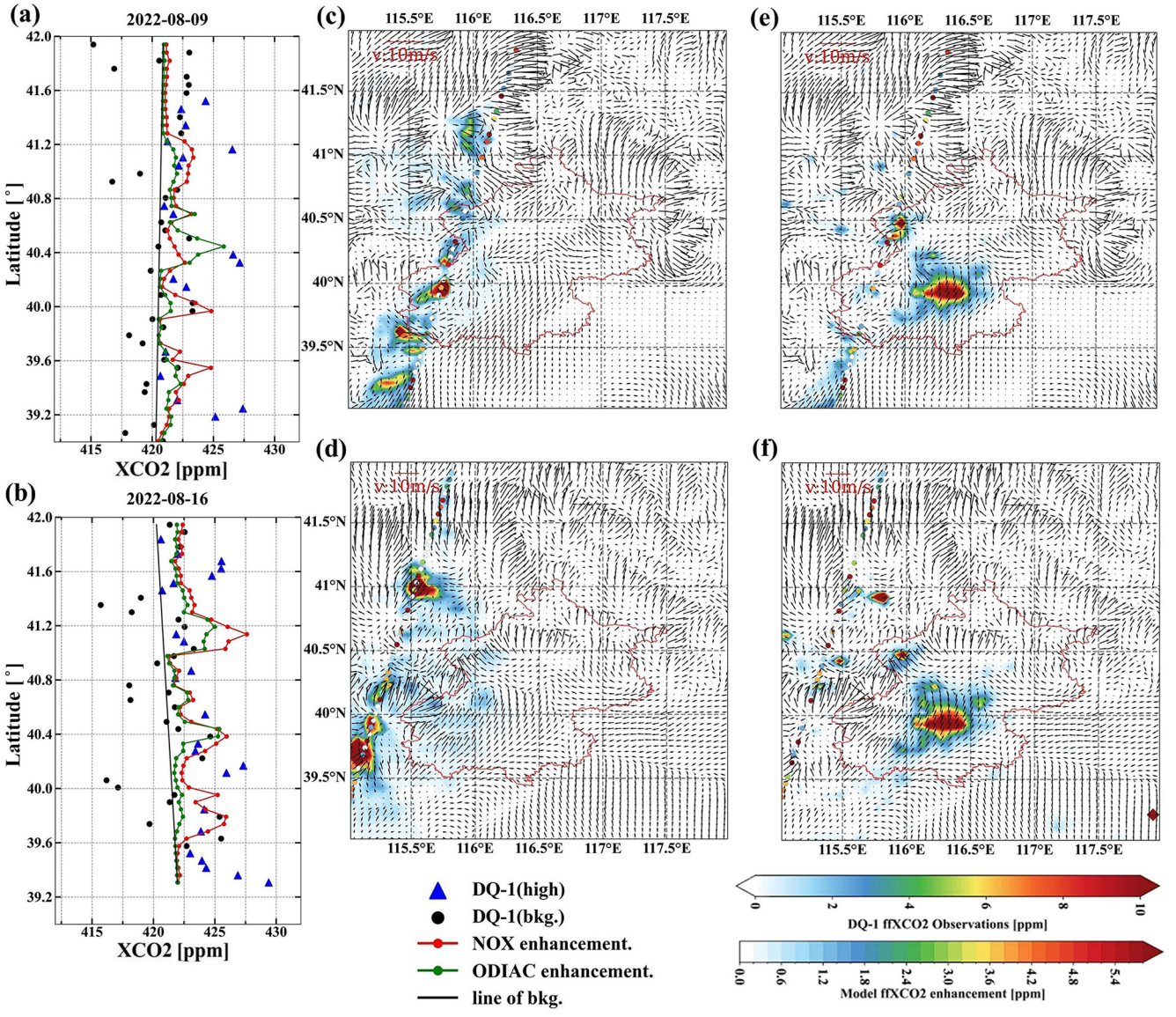

Figure 7. Similar to Fig. 5, comparison between simulated and observed ffXCO_2 enhancements using DQ-1 overpasses above Beijing on 9 August 2022 at 18:00 UTC **(a, c, e)** and 16 August 2022 at 18:00 UTC **(b, d, f)**. Panels **(c)**, **(d)** show the simulated ffXCO_2 enhancements based on the NO_x emissions, while panels **(e)**, **(f)** show those based on the ODIAC inventory.

tently greater than 3 m s^{-1}. Under such meteorological conditions, the posterior estimates represent emissions from several hours prior to satellite overpass. The posterior uncertainties of the CO_2-to-NO_x ratio were 15.09 %–18.86 % for Cairo, 14.72 %–18.67 % for Paris, and 14.08 %–16.24 % for Beijing. Overall, uncertainties were larger for Cairo and Paris compared with Beijing.

As described in Sect. 4.1, the prior uncertainty of the CO_2-to-NO_x ratio was prescribed based on available statistics and emission characteristics. Owing to more comprehensive statistics and advanced manufacturing processes, large metropolitan areas typically exhibit better-characterized emission features. Accordingly, the prior uncertainties for Beijing and Paris were smaller than those for Cairo. Table 2 further shows that the relative contributions of observational and transport errors differed across cities. In Cairo, transport errors dominated over observational errors, whereas in Paris the opposite held true. For Beijing, the relative magnitudes of transport and observational errors varied across orbits. The overall smaller posterior uncertainty for Beijing compared to Cairo and Paris reflects its more stable prior emission characteristics.

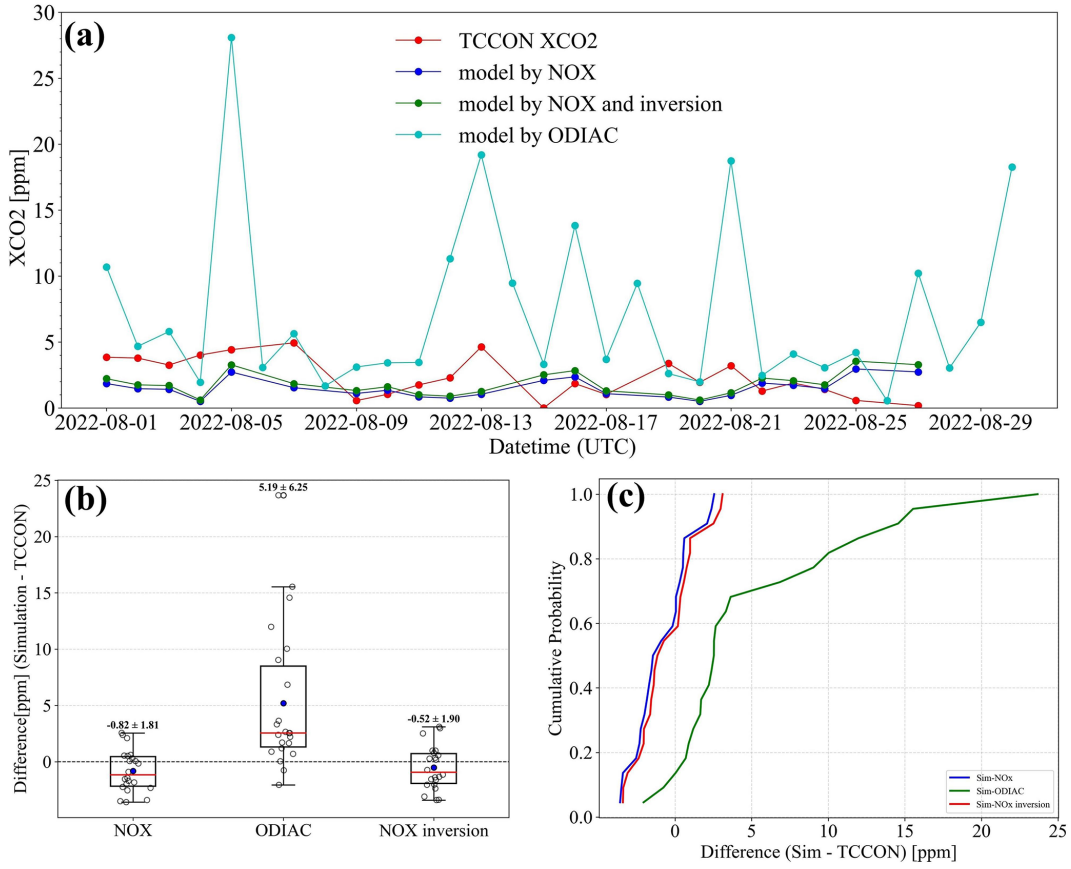

Figure 8. Comparison of ffXCO_2 observed at the TCCON Xianghe site in Beijing during August with ffXCO_2 simulated using the NO_x inventory and the ODIAC inventory. Panel **(a)** shows the ffXCO_2 observed by TCCON (red line), simulated ffXCO_2 using the NO_x emissions (dark blue line), simulated ffXCO_2 using the ODIAC inventory (light blue line), and simulated ffXCO_2 using the posterior NO_x emissions (green line). Panel **(b)** presents the distribution of differences between simulated ffXCO_2 (from the NO_x and ODIAC inventories) and TCCON observations throughout August, with bold numbers indicating the mean and standard deviation. Panel **(c)** shows the cumulative probability distributions of the differences between simulated ffXCO_2 (NO_x emissions and ODIAC inventory) and TCCON observations.

3.3 The Uncertainty of Transport Model

Atmospheric transport modeling uncertainty has been recognized as a major factor affecting emission constraints (Wu et al., 2018). Systematic errors arising from a combination of transport model biases and misrepresented statistical inputs can reduce the magnitude and spatial coverage of terrestrial uncertainty reductions by roughly a factor of two. Notably, transport-related uncertainties in ffXCO_2 represent a key source of error in inverse emission estimates (Ye et al., 2020). In this section, we quantify the impact of transport errors on simulated XCO_2 arising from uncertainties in horizontal wind fields and vertical mixing, with a focus on their influence on the inversion of ffXCO_2 fluxes.

Errors induced by wind field uncertainties propagate through the model and affect the accuracy of CO_2 emission estimates (Sheng et al., 2025). Previous studies have accounted for column transport errors by weighting variance relative to pressure and treating each model level independently (Lin and Gerbig, 2005; Wu et al., 2018). Ye et al. (2020) further quantified ffXCO_2 simulation uncertainty by introducing random perturbations in wind speed and direction (Ye et al., 2020). Building on these approaches, we investigate how horizontal wind speed and wind direction errors influence inversion performance.

Here, horizontal transport error is propagated through the model via its effect on ffXCO_2 plume dispersion (Luo et al., 2026; Qu et al., 2026). For the selected cities, errors are assumed to be unbiased. Wind direction uncertainty is represented by rotating the plume around the emission center, followed by the addition of random wind speed perturbations to the rotated plume. Using DQ-1 wind field data, random errors were added at each model level (wind direction perturbation between $-10°$ and $10°$, wind speed perturbation between -1 and $1\,m\,s^{-1}$), and the STILT footprints were recomputed to obtain plume-averaged footprints with random errors included (Yi et al., 2025a).

In total, 10^4 simulations were conducted, with the ffXCO_2 integrated along each satellite track. The standard deviation

Figure 9. Monthly mean wind rose plots for Cairo, Paris, and Beijing in August.

(1σ) of these simulations is used to represent the uncertainty in simulated ffXCO_2 resulting from horizontal transport errors (Fig. 10).

Figure 10 presents the total simulated ffXCO_2 along DQ-1 overpasses for the different study regions. Overall, the simulated ffXCO_2 totals for the three cities are of comparable magnitude. Notably, compared with Beijing and Cairo, the horizontal transport uncertainty along the two Parisian tracks is the lowest, at 0.36 and 0.76 ppm, respectively. In Cairo, the satellite tracks traverse the edges of emission plumes, making the simulations highly sensitive to wind speed and direction, which results in larger transport model errors. Beijing, with its complex terrain and variable wind fields, exhibits more intricate transport uncertainties relative to the other two cities. These observations indicate that transport model uncertainty is closely related to city-scale emissions, the relative alignment of plumes and satellite tracks, model performance, and local topography. Variations in these factors contribute to temporal changes in posterior emission uncertainties along different tracks.

Vertical turbulent mixing governs the vertical transport of air parcels and controls the dilution of surface emissions within the boundary layer (Vertical mixing in atmospheric tracer transport models: error characterization and propagation). Although column-integrated measurements may be less sensitive to the vertical distribution of tracers than in situ observations, errors in planetary boundary layer (PBL) height can still affect column simulations due to wind shear

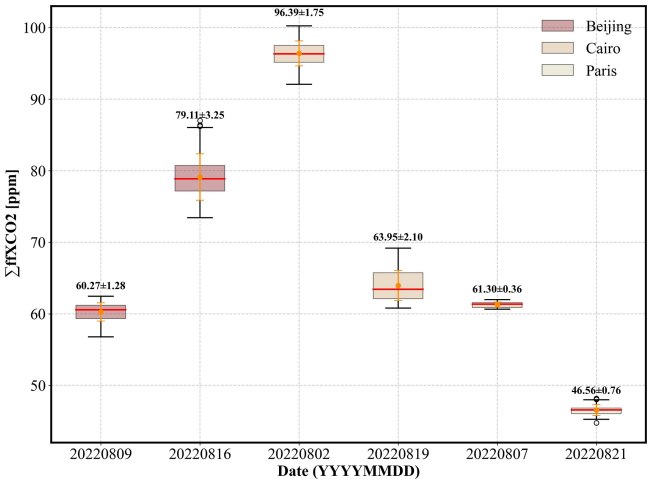

Figure 10. Boxplots of modeled integrated ffXCO_2 enhancements ffXCO_2 along selected DQ-1 overpasses for the three cities (distinguished by box color) with dates labeled on the x-axis. For each box, the central line represents the median (q2), and the bottom and top edges represent the 25th and 75th percentiles (q1 and q3), respectively. Whiskers extend to the minimum and maximum values. Numbers indicate the mean ± standard deviation.

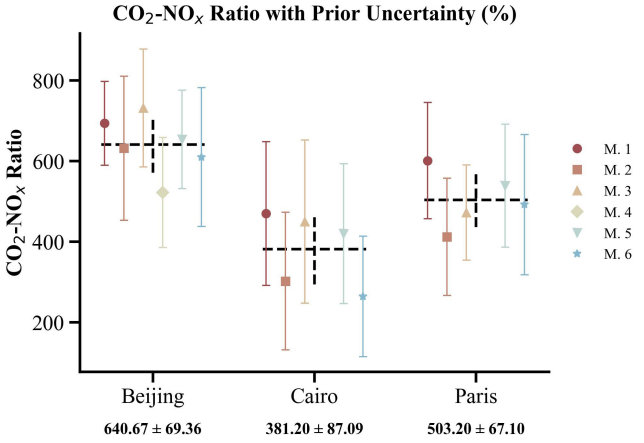

Figure 11. Results of CO_2-to-NO_x ratios obtained using different calculation methods for Beijing, Cairo, and Paris. Different CO_2-to-NO_x ratios within the same city are distinguished by color. Additionally, the mean and standard deviation of the different ratios for each city are also shown.

and its interaction with vertical redistribution of tracers (Planetary boundary layer errors in mesoscale inversions of column-integrated CO_2 measurements). It is worth noting that the ACDL instrument includes an aerosol channel capable of providing extinction coefficient profiles and planetary boundary layer height (PBLH) products (Dai et al., 2024). In this study, PBLH data derived from ACDL retrievals are used in the simulations, helping to mitigate errors arising from inaccurate boundary layer height assumptions. Therefore, boundary layer height errors are not considered in the estimation of ffXCO_2.

4 Importance of Satellite Observations for Optimizing the CO_2-to-NO_x Ratio

4.1 Variations in CO_2-to-NO_x ratio calculation methods

We systematically accounted for the uncertainties associated with the prior CO_2-to-NO_x ratios for each method (see Sect. 2.2.1 (4) M1–M6). The uncertainty of the CO_2-to-NO_x ratio arises from the uncertainties of the underlying emissions. For Method 1, a Monte Carlo simulation was performed: CO_2 and NO_x inventory uncertainties (Wang et al., 2013) were used to generate random perturbations at each grid, and the CO_2-to-NO_x ratio was recalculated 10 000 times to obtain the distribution characteristics. The prior CO_2-to-NO_x ratio uncertainty was expressed as R90/M, where R90 is the range between the 95th and 5th percentiles and M is the median value from 10 000 Monte Carlo simulations. For Method 2, the uncertainty was represented as:

$$\sigma_{C/N} = \sqrt[2]{\sigma^2_{NO_x} + \sigma^2_{ffCO_2}} \quad (14)$$

where σ_{NO_x} and σ_{ffCO_2} denote the uncertainties of the NO_x and ffCO_2 emission factors, respectively. Notably, for each method, the use of different inventories requires adjustment of the assigned uncertainties (see Appendix A6). In Method 3, the prior CO_2-to-NO_x ratio uncertainty was derived from the quadratic sum of observational uncertainties in NO_2 and CO_2 concentrations and the Gaussian fitting uncertainty.

In this section, we used six different CO_2-to-NO_x ratio calculation methods to estimate the city-scale ratios for Beijing, Cairo, and Paris in August. Since the MEIC inventory is only available for Beijing, six prior CO_2-to-NO_x ratios were obtained for Beijing, while five ratios were derived for Paris and Cairo. Figure 11 presents the CO_2-to-NO_x ratios and their associated uncertainties for each city using the different methods. We also calculated the mean and standard deviation of the ratios across methods for each city, reflecting both the overall understanding of the city-scale prior CO_2-to-NO_x ratio and the variability arising from methodological differences.

The results consistently show the ordering Beijing > Paris > Cairo. Moreover, more developed cities typically have better production technologies and more detailed emission statistics (Oda et al., 2019; Ye et al., 2020). Consequently, the prior uncertainties for Beijing and Paris are notably smaller than those for Cairo, and the variability of CO_2-to-NO_x ratios across methods is also reduced for these cities.

4.2 Bayesian Inversion for Reducing CO_2-to-NO_x Ratio Uncertainty

Using different prior CO_2-to-NO_x ratios, we conducted the Bayesian inversion described in Sect. 2.2.2 to optimize the August CO_2-to-NO_x ratios for Beijing, Cairo, and Paris along the respective DQ-1 satellite overpasses. Figure 12 shows the absolute reduction in posterior uncertainty (posterior minus prior) and the relative reduction (prior minus posterior, divided by prior) for each city across different orbits. For Beijing, the posterior uncertainty decreased by 9.75 %–20.88 %, corresponding to a 31.4 %–56.49 % reduction relative to the prior. In Cairo, the posterior uncertainty decreased by 21.74 %–38.87 %, equivalent to a 51.8 %–66.63 % reduction, while in Paris the reduction ranged from 11.24 %–20.09 %, corresponding to a 34.22 %–51.13 % decrease relative to the prior.

These results indicate that, for all cities, the posterior uncertainties were significantly reduced regardless of the method used to calculate the prior ratio. This demonstrates that constraining the inversion with DQ-1 ACDL observations substantially improves the accuracy of $ffCO_2$ estimates derived from NO_x emissions. Notably, in Cairo – the city with the largest prior uncertainty – the reduction in uncertainty after constraining with both active and passive satellite observations was the greatest, highlighting the effectiveness of satellite data in mitigating emission uncertainties in cities with incomplete statistical information. These findings underscore the potential of satellite remote sensing to supplement emission inventories and enhance the reliability of urban emission estimates.

Furthermore, we examined the range of CO_2-to-NO_x ratios calculated for each city using different methods (Fig. 13). In the figure, the black boxes represent the prior distribution ranges, while the red boxes indicate the posterior distribution ranges. The distribution ranges illustrate the variability among CO_2-to-NO_x ratios obtained from different methods, and we also quantified the reduction of the posterior range relative to the prior. Except for the orbit over Paris on 21 August, all other results show that the posterior ranges were reduced by more than 60 % compared to the priors.

These results demonstrate that our approach effectively reduces the discrepancies arising from different CO_2-to-NO_x ratio calculation methods. That is, prior ratios derived from various methods are constrained to approximately the same range after inversion. This finding underscores the importance of using observational constraints to obtain more accurate CO_2-to-NO_x ratios in future $ffCO_2$ emission estimations.

5 Summary

Accurate identification and quantification of anthropogenic CO_2 emissions form a critical scientific basis for national emission reduction policies and carbon sink strategies. However, bottom-up inventory approaches typically operate on long compilation cycles (e.g., annual), making it difficult to capture short-term or near-real-time emission dynamics. Most inventories provide only annual totals and lack the temporal resolution needed to characterize daily, hourly, or event-driven emissions.

In this study, we developed a city-scale $ffCO_2$ inversion framework that integrates both active and passive satellite observations of greenhouse gases. This framework enables high-resolution estimation of fossil fuel emissions at satellite overpass times and over preceding hours, while simultaneously constraining the city-scale CO_2-to-NO_x ratio. A key feature of the approach is its reduced reliance on prior emission inventories, allowing rapid and objective identification and quantification of anthropogenic emission signals at regional scales, thereby enhancing the monitoring and verification of urban emission dynamics. In this framework, satellite-observed XCO_2 enhancements attributed to urban emissions are used to constrain WRF-STILT atmospheric transport simulations of anthropogenic CO_2. This process not only enables quantitative assessment of urban fossil fuel emissions but also provides independent evidence for improving emission inventories and refining urban carbon accounting systems. The study highlights the potential of combining multi-source satellite observations with transport models and lays a foundation for future city-scale $ffCO_2$ inversions based on the CO_2-to-NO_x ratio. Furthermore, we discuss the impact of the lack of standardized CO_2-to-NO_x ratio calculation methods on urban emission estimates and demonstrate that observational constraints on city-scale ratios can substantially improve $ffCO_2$ estimation from a carbon-nitrogen co-optimization perspective. Using a Bayesian inversion approach, we optimized the CO_2-to-NO_x ratios for Cairo, Paris, and Beijing in August 2022 based on DQ-1 satellite overpasses and estimated the cities' fossil fuel CO_2 emissions using TROPOMI NO_2 data. The resulting CO_2-to-NO_x ratios ranged from 428–512, 731–742, and 553–640 for Cairo, Paris, and Beijing, respectively, indicating significant day-to-day variability in emission estimates. Cairo exhibited the largest posterior uncertainty, primarily due to high prior uncertainty and transport model errors. Differences in posterior uncertainties across orbits were also closely related to meteorological conditions and the relative position of the satellite tracks to urban plumes. We further compared $ffXCO_2$ enhancement distributions simulated using the ODIAC inventory. Results for Cairo and Paris were broadly consistent with TROPOMI-based simulations, while notable differences emerged for Beijing. TCCON XCO_2 observations were used to interpret these discrepancies. The monthly mean $ffXCO_2$ enhancement derived from TROPOMI NO_2 data differed from TCCON measurements by less than 1 ppm, whereas the ODIAC-based results deviated by 5.16 ppm. This highlights the need to account for uncertainties arising from inventory allocation and outdated updates when interpreting XCO_2 inversion re-

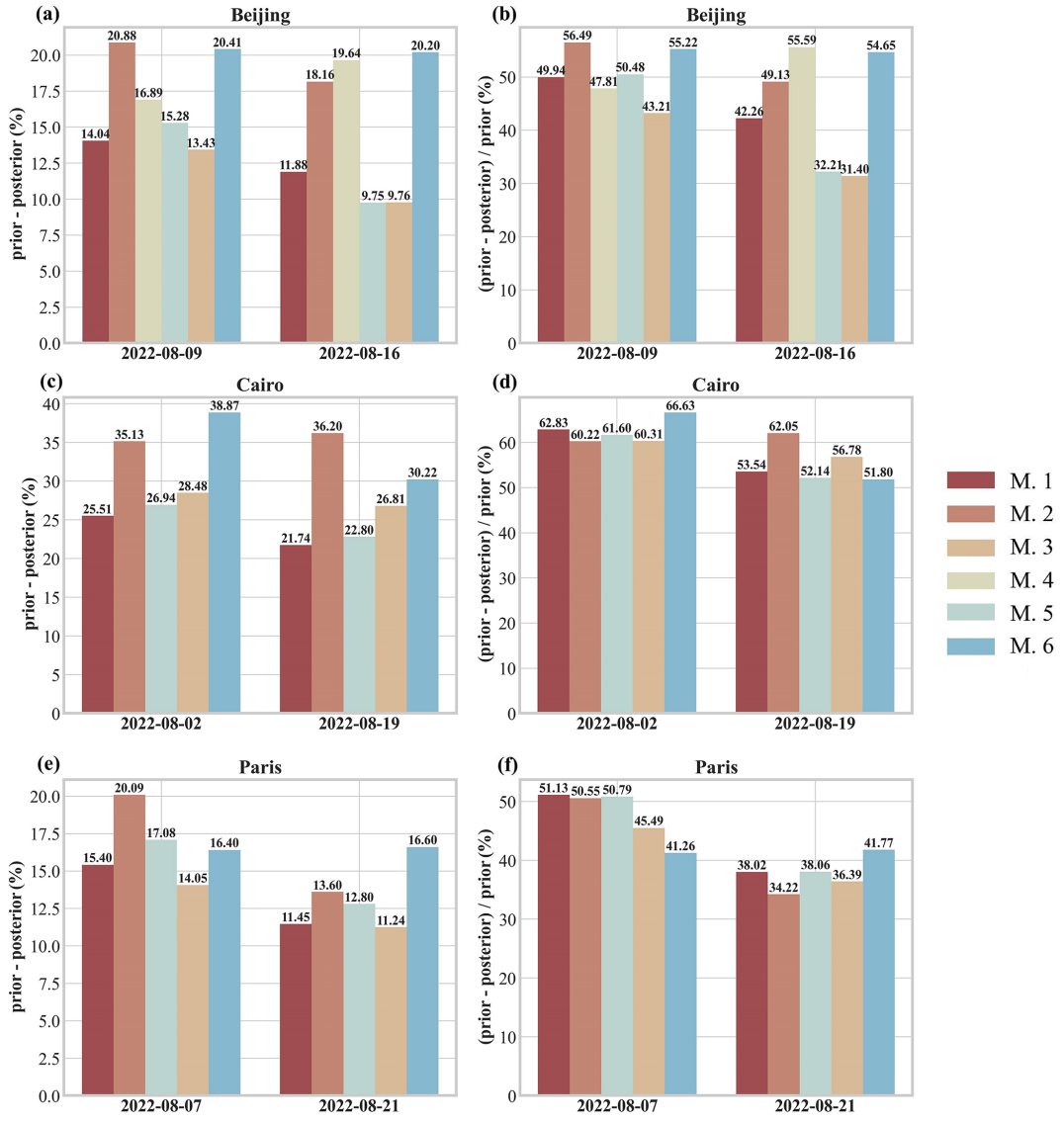

Figure 12. Comparison of Bayesian inversion prior and posterior uncertainties for each orbit over different cities. Panels **(a)**, **(c)**, **(e)** show the absolute reduction in uncertainty (prior uncertainty minus posterior uncertainty), while panels **(b)**, **(d**, **(f)** show the relative reduction in uncertainty (prior minus posterior uncertainty divided by prior uncertainty). Results from different prior CO_2-to-NO_x ratios are represented by bars in different colors, with the values displayed at the top of each bar.

sults. We systematically examined the impact of different prior CO_2-to-NO_x ratio calculation methods on urban $ffCO_2$ inversions. In our study, methodological differences led to variations of 10.8 %–22.8 % in prior ratios. Importantly, regardless of the prior ratio or its uncertainty, DQ-1 observations constrained the posterior values to a similar range, substantially reducing discrepancies among different calculation methods. Another limitation concerns the uncertainty of the divergence-derived NO_x emissions. Although monthly averaging reduces random noise, it does not guarantee that daily divergence errors average to zero. Sampling biases related to clouds, aerosols, surface reflectance, and photochemical variability may persist in the monthly mean. Moreover, gradient operations can amplify white noise in the NO_2 column field and generate structured artifacts in the derived fluxes. Therefore, the current uncertainty estimates should be interpreted as lower-bound, first-order uncertainty estimates. Future work should include more explicit noise-filtering and detection-limit analyses, ideally using ensemble perturbations of the original Level-2 NO_2 observations and high-resolution chemical transport simulations to better represent NO_2 profile shapes, lifetimes, and NO_x:NO_2 conversion factors (Cifuentes et al., 2025; Guan et al., 2026; Wang et al., 2025; Zhang et al., 2026)

Looking ahead, improving satellite-based city-scale $ffCO_2$ inversions will require accounting for the spatiotemporal cor-

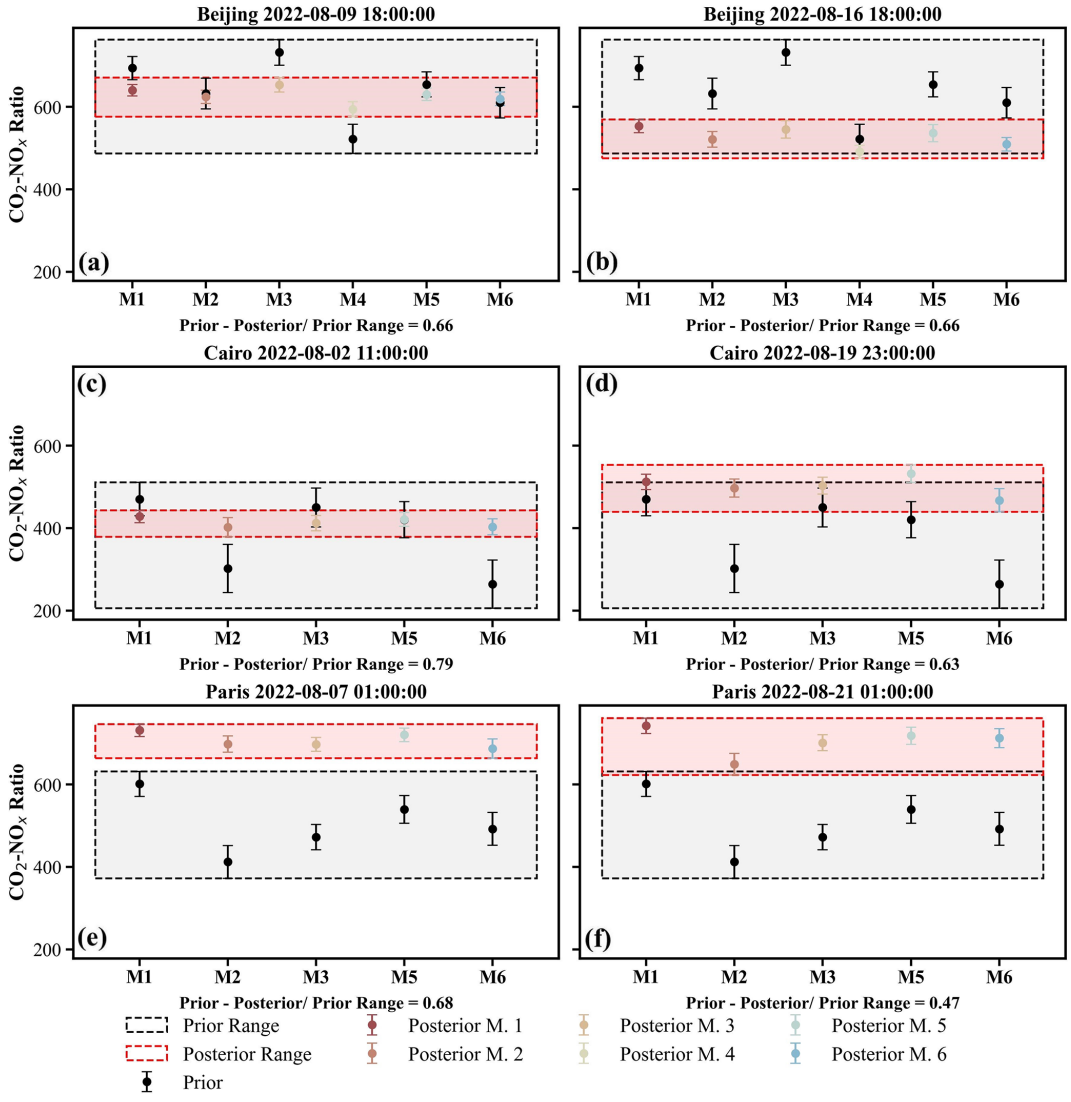

Figure 13. Distribution ranges of prior and posterior CO_2-to-NO_x ratios calculated using different methods. Black boxes represent the range of prior CO_2-to-NO_x ratios, with posterior ratios indicated by black circles. Red boxes represent the range of posterior CO_2-to-NO_x ratios, with posterior uncertainties from different methods shown using different colors and symbols.

relations of prior emission errors. Our current framework does not yet incorporate this aspect, which imposes certain limitations on the interpretation and application of the results. Satellite observations are inherently constrained by inversion errors, sampling geometry, and revisit frequency, limiting overpass opportunities. A single prior factor, such as a uniform CO_2-to-NO_x ratio, cannot fully capture the complex spatiotemporal features of emissions. Incorporating prior error correlations can mitigate uncertainties arising from sparse observations and better resolve temporal and spatial variability in urban emissions. Moreover, the number of satellite tracks required to constrain city emissions depends on the desired emission resolution and uncertainty thresholds relevant for policy applications. Lower temporal resolution may suffice for long-term trend analysis, whereas capturing short-term peaks or episodic emissions necessitates higher observation frequency and precision. This consideration aligns with emerging international approaches emphasizing multi-platform, multi-temporal observations, combining polar-orbiting, geostationary satellites, and ground-based monitoring to achieve multidimensional constraints on urban emissions.

Overall, our results demonstrate that coupling high-resolution atmospheric transport simulations with a Bayesian inversion framework allows TROPOMI and DQ-1 multi-source observations to effectively constrain urban ffXCO_2 enhancement signals. The approach captures spatial heterogeneity of emissions, particularly in cities with strong emission intensities and well-defined plume structures, providing a robust basis for quantitative analysis. Furthermore, current

methods estimating $ffCO_2$ from NO_x emissions often lack explicit treatment of CO_2-to-NO_x ratio uncertainty, which can significantly influence inversion outcomes. Differences among calculation methods for the same region can be as large as 258–304. Notably, our inversion framework substantially reduces CO_2-to-NO_x ratio uncertainty, providing more stable priors for urban $ffCO_2$ estimation. Recent studies suggest the need to further optimize CO_2-to-NO_x emission ratios at regional scales to improve $ffCO_2$ estimates (Feng et al., 2024). Therefore, we recommend that future NO_x-based $ffCO_2$ inversion studies adopt observational constraints to refine CO_2-to-NO_x ratios, minimizing errors arising from prior ratio uncertainties.

Appendix A

A1 ACDL XCO_2 Data Inversion

Unlike passive satellite XCO_2 products (e.g., OCO-2/3), the DQ-1 XCO_2 product – hereafter referred to as XCO_2^{Lidar} to distinguish it from passive measurements – is derived from the differential absorption between ACDL's on-band wavelength (strong CO_2 absorption) and off-band wavelength (weak CO_2 absorption). Here, "WF(p)" refers to the lidar signal and integrated weighting function introduced in Sect. 2.1.1, with "p" representing atmospheric pressure:

$$XCO_2^{\mathrm{Lidar}} = \frac{2 \times \ln\left(\frac{V_{\mathrm{off}} \times V_{\mathrm{on}-0}}{V_{\mathrm{on}} \times V_{\mathrm{off}-0}}\right)}{\int_{\mathrm{p\_surface}}^{\mathrm{p\_toa}} \mathrm{WF(p)d}p} \tag{A1}$$

here, V_{on} and V_{off} denote the reflected signal energies at the on-band and off-band wavelengths, respectively, while $V_{\mathrm{on}-0}$ and $V_{\mathrm{off}-0}$ correspond to the transmitted signal energies. p_surface represents the atmospheric pressure at the sub-satellite point of the laser, and p_toa denotes the pressure at the top of the atmosphere. The denominator in Eq. (A1) represents the integrated weighting function (WF(p)), which can be expressed according to Refaat et al. (2016) as:

$$\mathrm{WF(p)} = \Delta\sigma_{\mathrm{wf}}(\lambda_{\mathrm{on}}, \lambda_{\mathrm{off}}, p) \times N_{\mathrm{dry}}(p) \tag{A2}$$

here, $\Delta\sigma_{\mathrm{wf}}(\lambda_{\mathrm{on}}, \lambda_{\mathrm{off}}, p)$ represents the differential absorption cross-section of CO_2 between the on-band λ_{on} and off-band λ_{off} wavelengths at pressure p. N_{dry} denotes the number of dry air molecules per unit area within the corresponding pressure layer.

A2 Derivation of the Principle of Mass Balance

For satellite column observations of specific species such as NO_2, the mass balance equation can be expressed as follows:

$$\begin{cases} \frac{\partial V_{\mathrm{NO_2}}}{\partial t} + \nabla \times \boldsymbol{F}_{\mathrm{NO_2}} = E_{\mathrm{NO_2}} - S \\ \boldsymbol{F}_{\mathrm{NO_2}} = V_{\mathrm{NO_2}} \boldsymbol{u}_{100} \\ S \approx \frac{V_{\mathrm{NO_2}}}{\tau} \end{cases} \tag{A3}$$

Table A1. DQ-1 ACDL operating parameters.

Parameters	Values
Oribit altitude	705 km
Lidar footprint diameter	~ 70 m
Horizontal spacing of lidar footprints	~ 350 m
Field of view	< 0.2 mrad
Telescope diameter	1000 nm
Divergence angle after laser beam expansion	< 0.1 mrad
Repetition frequency	20 Hz
Laser pulse width	< 50 ns
Laser energy	75 mJ
Off-line wavelength	1572.085 nm
On-line wavelength	1572.024 nm

here, $V_{\mathrm{NO_2}}$ represents the columnar NO_2 concentration observed by TROPOMI, defined as a scalar function of x and $\nabla = (\partial/\partial x, \partial/\partial y)$ denotes the gradient operator; $= \boldsymbol{F}_{\mathrm{NO_2}}(F_x, F_y)^{\mathrm{T}}$ is the horizontal flux, with units of $\mathrm{mol\,m^{-2}\,s^{-1}}$, expressed as a vector function of x and y and weighted by the wind vector. The 100 m wind field is commonly used to characterize horizontal transport within the planetary boundary layer (PBL, Sun, 2022). τ represents the first-order chemical lifetime of NO_2 in seconds.

By solving the system of equations in Eq. (A3) and expanding the horizontal flux divergence using vector calculus, we obtain the derivation of Eq. (A4) from Eq. (A3):

$$\begin{cases} \boldsymbol{u}_{100} \times (\nabla V_{\mathrm{NO}}) + V_{\mathrm{NO}}(\nabla \times \boldsymbol{u}_{100}) = \nabla \times \boldsymbol{F}_{\mathrm{NO_2}} \\ E_{\mathrm{NO_2}} = \frac{\partial V_{\mathrm{NO_2}}}{\partial t} + \nabla \times \boldsymbol{F}_{\mathrm{NO_2}} + \frac{V_{\mathrm{NO}}}{\tau} \end{cases} \tag{A4}$$

Sun (2022), in their first-principles derivation, introduced a "topographic correction term" to replace the wind divergence term $V_{\mathrm{NO}}(\nabla \times \boldsymbol{u}_{100})$. Beirle et al. (2023) demonstrated that incorporating a topographic correction significantly improves the inversion of power-plant NO_x emissions based on the divergence method. Koene et al. (2024) carefully compared these two terms in the derivation of the divergence method, showing that they originate from the continuity equations of the source and non-source terms, and that numerically, the wind divergence and wind–topography terms are approximately equal in the absence of observational errors.

Despite their numerical equivalence in derivation, the accuracy of reanalyzed wind fields is generally lower than that of surface elevation data. Therefore, in practical measurements – particularly in complex, fine-scale settings – the wind divergence term alone may not provide sufficient constraint. Correcting wind divergence artifacts using topographic gradients is more feasible, especially in regions with rugged terrain. Accordingly, we revise Eq. (A5) using Eq. (A4) as follows:

$$\frac{V_{\mathrm{NO_2}} \boldsymbol{u}_{10} \times (\nabla z_0)}{H} \approx V_{\mathrm{NO_2}}(\nabla \times \boldsymbol{u}_{100}) \tag{A5}$$

Table A2. Model version information used in this study.

Model	Version
STILT (Stochastic Time-Inverted Lagrangian Transport)	V2
WRF (Weather Research and Forecasting)	V4.0
X-STILT (X-Stochastic Time-Inverted Lagrangian Transport model)	V1

here, $\frac{V_{NO_2}\boldsymbol{u}_{10}\times(\nabla z_0)}{H}$ represents the topographic correction term, where the 10 m wind is approximated as the near-surface wind, and H denotes the gas scale height in meters. Following previous studies (Beirle et al., 2023; Sun, 2022; Liu et al., 2021), Eq. (A5) is assimilated over both temporal and spatial dimensions. This procedure is concisely represented using the operator $\langle f \rangle$, as introduced in the derivations by Liu et al. and Sun et al. Ultimately, this approach allows the derivation of the vertical NO_2 flux on a grid-resolved basis.

A3 Atmospheric Model Setting

In this study's application of STILT, hourly outputs from version 4.0 of WRF are used to provide high resolution meteorological fields, with the model grid configured to 32 vertical (eta) layers. The 6 hourly NCEP FNL (Final) global operational analysis data (ds083.3, $0.25°\times0.25°$) are used as initial and boundary conditions for meteorological and land surface fields to provide the initial and boundary conditions for WRF runs. The simulations run for 30 h, but only the 7th to 30th hours of each simulation are used to avoid spin-up effects in the first 6 h.

In this study, we used the STILT model, version 2, to simulate atmospheric transport processes. STILT is configured to release 500 particles per receptor each time, with forward dispersion over 24 h. The particle release heights for STILT are set within the range of 50–1000 m, with releases every 50 m, and 1000–2000 m, with releases every 100 m, the spatial resolution of the STILT simulations is 1 km × 1 km. Generally, as MAXAGL increases from 1–2 km, the urban enhancement increases and then stabilizes.

A4 Calculation of NEE XCO_2 enhancement

We performed vertical integration following the method provided by the TCCON team, using the 51 altitude levels listed in the publicly available ak_altitude dataset, which also serve as input heights for the STILT model. In contrast to the XSTILT calculation method used for DQ-1, we applied the integration operator integration_operator_x2019 together with the mean averaging kernel ak_xco2 to the STILT footprints across the 51 levels in order to generate the simulated XSTILT values required for this study. We selected the National Institute for Environmental Studies (Japan) data-driven Upscale Product of Global Gross Primary Production (NEE) as the reference for the overall local NEE during the DQ-1 overpasses. By convolving the NEE inventory with XSTILT, we simulated the XCO_2 enhancement at TCCON sites attributable to NEE.

A5 Calculation of Priori NO_x Emission Uncertainty

The uncertainty estimated here should be regarded as a first-order propagated uncertainty rather than the full uncertainty of the divergence-derived NO_x emissions. In particular, this formulation does not fully capture structured errors arising from finite-difference gradient operators, oversampling from Level-2 observations to Level-3 grids, non-Gaussian retrieval noise, or sampling biases caused by clouds, aerosols, surface reflectance, and photochemical variability. The uncertainty of the NO_x inventory derived from the mass balance approach can be estimated using the error propagation law as follows:

$$\varepsilon_{NO_x} = \sqrt[2]{\varepsilon_{\alpha}^2 + \varepsilon_{NO}^2} \tag{A6}$$

where ε_{α} represents the uncertainty in the NO_x/NO_2 ratio, its uncertainty arises from the uncertainties in the input parameters of the chemical model (Liu et al., 2022). And ε_{NO_2} denotes the uncertainty in the NO_2 flux field. The latter can be further decomposed as:

$$\varepsilon_{NO} = \sqrt[2]{\varepsilon_{TROPOMI}^2 + \varepsilon_{Wind}^2 + \varepsilon_{Fit}^2} \tag{A7}$$

here, $\varepsilon_{TROPOMI}$ is the uncertainty of the NO_2 column concentration, ε_{Wind} represents the uncertainty associated with the wind field, and ε_{Fit} accounts for the uncertainty in the fitted vertical scale height and chemical lifetime. The uncertainty of NO_2 arises from multiple factors, including spectral fitting, stratospheric correction, AMF, clouds, vertical profiles, and surface albedo (Boersma et al., 2018; Verhoelst et al., 2021; Van Geffen et al., 2022; Lu et al., 2025). In this study, we use the ratio of the standard deviation to the mean of the column concentration within the study area as a proxy for the TROPOMI observational noise, integrated over the time series. It should be noted that this proxy is calculated based on the oversampled gridded data (also referred to as Level-3) rather than the original Level-2 orbit data. In this study, we do not account for errors introduced during the oversampling of TROPOMI L2 data to the grid (Glissenaar et al., 2025). With appropriate gridding, the uncertainty in polluted areas can be reduced by approximately 20 % compared with the original orbits (Sun et al., 2018a). Wind field uncertainty is quantified through 104 Monte Carlo perturbations of wind speed and direction, with the propagated standard deviation representing the flux variability. The fitting uncertainty is obtained by performing 104 Monte Carlo draws of the grids involved in the fit, generating ensembles of scale heights and chemical lifetimes, with the final fitting error defined as the root mean square of the standard deviations of these ensembles.

Table A3. The overall uncertainty of NO_x emissions and the uncertainties of individual components were derived using the dispersion model.

	NO_x/NO_2 uncertainty (%)	NO_2 uncertainty(%)	Wind uncertainty(%)	Fitted uncertainty(%)	Total uncertainty(%)
Beijing	6.51	15.49	16.76	1.67	23.79
Cairo	4.79	11.64	6.76	0.78	14.31
Paris	5.02	13.67	10.76	1.21	18.15

Using the method described above, we quantified the overall uncertainty of NO_x prior emissions for three cities, as well as the contributions from individual components, with the detailed results summarized in Table A3. It should be noted that the uncertainties reported here represent aggregated values for the entire urban area, rather than detailed uncertainties for individual grid cells.

Based on the uncertainty calculations, the total uncertainty is on the order of $\sim 24\,\%$ for Beijing, $\sim 18\,\%$ for Paris, and $\sim 14\,\%$ for Cairo. A closer look at the contributions of individual components reveals that NO_2 column concentrations and the wind field are the dominant sources, together accounting for more than 66.7 % of the total uncertainty. This is attributable to the nature of data-driven dispersion models, in which uncertainties in wind and concentration directly govern the overall uncertainty (Sun, 2022). The nonlinear gradient operations in dispersion models (e.g., second-order difference operators) can amplify white noise in the original concentration field, while in existing emission quantification models, wind fields are considered a major source of uncertainty due to sparse monitoring sites and model errors (Huang et al., 2025).

Among the three cities, NO_2 column inversion uncertainty is highest in Beijing. Unlike Cairo, where high surface reflectivity eases retrievals, Beijing is located in the highly polluted North China Plain with elevated AOD, which increases the difficulty of passive column inversion. In addition, Beijing's complex terrain contributes to the highest wind field uncertainty ($\sim 17\,\%$) among the three cities. The NO_x/NO_2 uncertainty is roughly similar across the three cities, consistent with previous studies using NU-WRF ($\sim 1.4 \pm 0.1$). In contrast, the uncertainty associated with first-order chemical lifetime and vertical scale height is the lowest among all components ($\sim 1\,\%$). This is different from earlier studies ($\sim 15\,\%$) (Liu et al., 2022) and reflects the benefit of the data-driven fitting approach proposed by Sun et al. (2018b) (see main text). Since no new assumptions were introduced in the current study, this uncertainty arises solely from the linear fitting model.

A6 Optimization results of the CO_2-to-NO_x ratio obtained using different calculation methods

Table A4. Inversion results of CO_2-to-NO_x ratios calculated using different methods.

Method	City	Date	Prior CO_2-to-NO_x ratio (λ)	CO_2-to-NO_x ratio uncertainty (%)	NO_x emission uncertainty (%)	Prior uncertainty (%)	Posterior CO_2-to-NO_x ratio (λ)	Posterior uncertainty (%)
1	Beijing	9 August 2022	694	15	23.79	28.12	640	14.08
	Beijing	16 August 2022	694	15	23.79	28.12	553	16.24
	Cairo	2 August 2022	470	37.99	14.31	40.60	428	15.09
	Cairo	19 August 2022	470	37.99	14.31	40.60	512	18.86
	Paris	7 August 2022	601	24.04	18.15	30.12	731	14.72
	Paris	21 August 2022	601	24.04	18.15	30.12	742	18.67
2	Beijing	9 August 2022	632	28.28	23.79	36.96	624	16.08
	Beijing	16 August 2022	632	28.28	23.79	36.96	521	18.8
	Cairo	2 August 2022	302	56.56	14.31	58.34	402	23.21
	Cairo	19 August 2022	302	56.56	14.31	58.34	497	22.14
	Paris	7 August 2022	412	35.35	18.15	39.74	698	19.65
	Paris	21 August 2022	412	35.35	18.15	39.74	649	26.14
3	Beijing	9 August 2022	732	20.02	23.79	31.09	653	17.65
	Beijing	16 August 2022	732	20.02	23.79	31.09	545	21.32
	Cairo	2 August 2022	450	45.81	14.31	47.99	412	18.74
	Cairo	19 August 2022	450	45.08	14.31	47.99	503	20.41
	Paris	7 August 2022	472	24.83	18.15	30.75	697	16.84
	Paris	21 August 2022	472	24.83	18.15	30.75	701	19.65
4	Beijing	9 August 2022	522	26.12	23.79	35.33	594	18.44
	Beijing	16 August 2022	522	26.12	23.79	35.33	491	15.69
5	Beijing	9 August 2022	654	18.72	23.79	30.27	630	14.99
	Beijing	16 August 2022	654	18.72	23.79	30.27	536	20.52
	Cairo	2 August 2022	420	41.32	14.31	43.73	421	16.79
	Cairo	19 August 2022	420	41.32	14.31	43.73	532	20.93
	Paris	7 August 2022	539	28.31	18.15	33.63	720	16.55
	Paris	21 August 2022	539	28.31	18.15	33.63	718	20.83
6	Beijing	9 August 2022	610	28.28	23.79	36.96	619	16.55
	Beijing	16 August 2022	610	28.28	23.79	36.96	509	16.76
	Cairo	2 August 2022	264	56.56	14.31	58.34	403	19.47
	Cairo	19 August 2022	264	56.56	14.31	58.34	467	28.12
	Paris	7 August 2022	492	35.35	18.15	39.74	687	23.34
	Paris	21 August 2022	492	35.35	18.15	39.74	712	23.14

A7 Posterior fossil fuel emissions distribution for each city

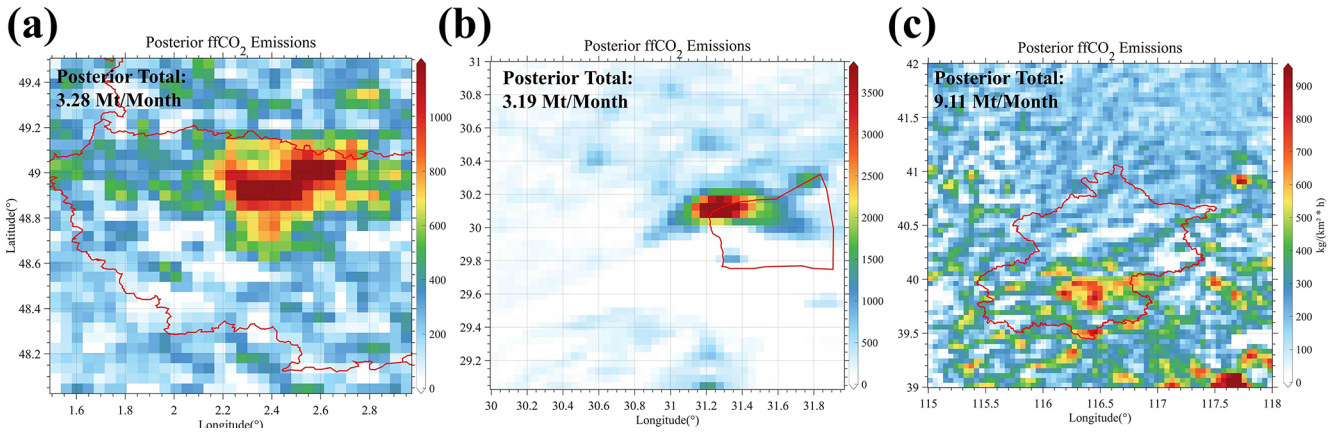

Figure A1. Posterior fossil fuel carbon dioxide emissions for each city. The red lines outline city boundaries, while the colored shading indicates carbon dioxide emission distribution.

Code availability. More information about the codes is available upon request.

Data availability. The DQ-1 ACDL productions underlying the results presented in this paper are not publicly available at this time but may be obtained from the authors upon reasonable request. The S5P-PAL dataset can be downloaded from https://data-portal.s5p-pal.com/ (last access: 29 January 2026). The National Centers for Environmental Prediction Final (NCEP FNL) operational global analysis dataset can be downloaded from https://doi.org/10.5065/D6M043C6 (National Centers for Environmental Prediction/National Weather Service/NOAA/U.S. Department of Commerce, 2000). The ds083.3 dataset can be downloaded from https://doi.org/10.5065/D65Q4T4Z (National Centers for Environmental Prediction/National Weather Service/NOAA/U.S. Department of Commerce, 2015). The ERA5 reanalysis dataset can be downloaded from https://doi.org/10.24381/cds.adbb2d47 (Copernicus Climate Change Service, Climate Data Store, 2023). The GMTED2010 dataset can be downloaded from https://www.usgs.gov/coastal-changes-and-impacts/gmted2010 (last access: 29 January 2026). The GEMS inventory can be downloaded from https://gems.sustech.edu.cn/data (last access: 29 January 2026). The Open-source Data Inventory for Atmospheric Carbon dioxide can be downloaded from https://db.cger.nies.go.jp/dataset/ODIAC/ (last access: 29 January 2026). The Emissions Database for Global Atmospheric Research can be downloaded from https://edgar.jrc.ec.europa.eu/emissions_data_and_maps (last access: 29 January 2026). The Multi-resolution Emission Inventory model for Climate and air pollution research can be downloaded from http://meicmodel.org.cn/ (last access: 29 January 2026).

Author contributions. The experiment design was made by GH and JY. The data collection was done by JY, YH, HL, GH. JY completed the design of the overall WRF-STILT model workflow, data collection, and result analysis. The data analysis was done by HZ, YZ, TS. WG and SL provide funding. The paper was written by JY and GH. All authors have reviewed, commented on, and approved the paper.

Competing interests. The contact author has declared that none of the authors has any competing interests.

Disclaimer. Publisher's note: Copernicus Publications remains neutral with regard to jurisdictional claims made in the text, published maps, institutional affiliations, or any other geographical representation in this paper. The authors bear the ultimate responsibility for providing appropriate place names. Views expressed in the text are those of the authors and do not necessarily reflect the views of the publisher.

Special issue statement. This article is part of the special issue "Greenhouse gas monitoring in the Asia–Pacific region (ACP/AMT/GMD inter-journal SI)". It is not associated with a conference.

Acknowledgements. The authors thank all the financial support for this research. This research was supported by the National Natural Science Foundation of China (grant-no.: 42475144), National Key R&D Program of China (grant-no.: 2024YFB3910203), and Beijing Natural Science Foundation (grant-no.: L211045).

Financial support. This research has been supported by the National Natural Science Foundation of China (grant no. 42475144) and the Fundamental Research Funds for the Central Universities (grant-no. 2042025kf0036).

Review statement. This paper was edited by Jason Cohen and reviewed by two anonymous referees.

References

Agency, I. E.: World energy outlook, OECD/IEA, Paris, https://www.iea.org/reports/world-energy-outlook-2009 (last access: 17 June 2026), 2009.

Beirle, S., Borger, C., Jost, A., and Wagner, T.: Improved catalog of NO_x point source emissions (version 2), Earth Syst. Sci. Data, 15, 3051–3073, https://doi.org/10.5194/essd-15-3051-2023, 2023.

Boersma, K. F., Eskes, H. J., Richter, A., De Smedt, I., Lorente, A., Beirle, S., van Geffen, J. H. G. M., Zara, M., Peters, E., Van Roozendael, M., Wagner, T., Maasakkers, J. D., van der A, R. J., Nightingale, J., De Rudder, A., Irie, H., Pinardi, G., Lambert, J.-C., and Compernolle, S. C.: Improving algorithms and uncertainty estimates for satellite NO_2 retrievals: results from the quality assurance for the essential climate variables (QA4ECV) project, Atmos. Meas. Tech., 11, 6651–6678, https://doi.org/10.5194/amt-11-6651-2018, 2018.

Che, K., Cai, Z., Liu, Y., Wu, L., Yang, D., Chen, Y., Meng, X., Zhou, M., Wang, J., Yao, L., and Wang, P.: Lagrangian inversion of anthropogenic CO_2 emissions from Beijing using differential column measurements, Environ. Res. Lett., 17, 075001, https://doi.org/10.1088/1748-9326/ac7477, 2022.

Che, K., Lauvaux, T., Taquet, N., Stremme, W., Xu, Y., Alberti, C., Lopez, M., García-Reynoso, A., Ciais, P., and Liu, Y.: CO_2 emissions estimate from Mexico City using ground-and space-based remote sensing, J. Geophys. Res.-Atmos., 129, e2024JD041297, 2024.

Cheng, C., Liu, D., Wang, S., Zhang, X., Zhang, L., Chen, W., Liu, J., Wan, X., Chen, W., and Chen, X.: Estimating strong point CO_2 emissions by combining spaceborne IPDA lidar and HSRL, Remote Sens. Environ., 328, 114898, 2025.

Cifuentes, F., Eskes, H., Dammers, E., Bryan, C., and Boersma, F.: Accurate space-based NO_x emission estimates with the flux divergence approach require fine-scale model information on local oxidation chemistry and profile shapes, Geosci. Model Dev., 18, 621–649, https://doi.org/10.5194/gmd-18-621-2025, 2025.

Copernicus Climate Change Service, Climate Data Store: ERA5 hourly data on single levels from 1940 to present, Copernicus Climate Change Service (C3S) Climate Data Store (CDS) [data set], https://doi.org/10.24381/cds.adbb2d47, 2023.

Crippa, M., Guizzardi, D., Muntean, M., Schaaf, E., Dentener, F., van Aardenne, J. A., Monni, S., Doering, U., Olivier, J. G. J., Pagliari, V., and Janssens-Maenhout, G.: Gridded emissions of air pollutants for the period 1970–2012 within EDGAR v4.3.2, Earth Syst. Sci. Data, 10, 1987–2013, https://doi.org/10.5194/essd-10-1987-2018, 2018.

Dai, G., Wu, S., Long, W., Liu, J., Xie, Y., Sun, K., Meng, F., Song, X., Huang, Z., and Chen, W.: Aerosol and cloud data processing and optical property retrieval algorithms for the spaceborne ACDL/DQ-1, Atmos. Meas. Tech., 17, 1879–1890, https://doi.org/10.5194/amt-17-1879-2024, 2024.

Danielson, J. J. and Gesch, D. B.: Global multi-resolution terrain elevation data 2010 (GMTED2010), US Geological Survey, 2331–1258, https://doi.org/10.3133/ofr20111073, 2011.

Dickerson, R. R., Stedman, D. H., and Delany, A. C.: Direct measurements of ozone and nitrogen dioxide photolysis rates in the troposphere, J. Geophys. Res.-Oceans, 87, 4933–4946, 1982.

Eldering, A., Wennberg, P., Crisp, D., Schimel, D., Gunson, M., Chatterjee, A., Liu, J., Schwandner, F., Sun, Y., and O'dell, C.: The Orbiting Carbon Observatory-2 early science investigations of regional carbon dioxide fluxes, Science, 358, eaam5745, 2017.

Feng, S., Jiang, F., Wang, H., Liu, Y., He, W., Wang, H., Shen, Y., Zhang, L., Jia, M., and Ju, W.: China's fossil fuel CO_2 emissions estimated using surface observations of coemitted NO_2, Environ. Sci. Technol., 58, 8299–8312, 2024.

Glissenaar, I., Boersma, K. F., Anglou, I., Rijsdijk, P., Verhoelst, T., Compernolle, S., Pinardi, G., Lambert, J.-C., Van Roozendael, M., and Eskes, H.: TROPOMI Level 3 tropospheric NO_2 dataset with advanced uncertainty analysis from the ESA CCI+ ECV precursor project, Earth Syst. Sci. Data, 17, 4627–4650, https://doi.org/10.5194/essd-17-4627-2025, 2025.

Guan, L., Cohen, J. B., Wang, S., Tiwari, P., Liu, Z., and Qin, K.: Improving aerosol absorption estimates via size-resolved constraints based on AERONET and in situ measurements, Geophys. Res. Lett., 53, e2025GL117418, https://doi.org/10.1029/2025GL117418, 2026.

Hakkarainen, J., Ialongo, I., and Tamminen, J.: Direct space-based observations of anthropogenic CO_2 emission areas from OCO-2, Geophys. Res. Lett., 43, 11,400–11,406, https://doi.org/10.1002/2016GL070885, 2016.

Han, G., Huang, Y., Shi, T., Zhang, H., Li, S., Zhang, H., Chen, W., Liu, J., and Gong, W.: Quantifying CO_2 emissions of power plants with Aerosols and Carbon Dioxide Lidar onboard DQ-1, Remote Sens. Environ., 313, 114368, https://doi.org/10.1016/j.rse.2024.114368, 2024.

Han, G., Wang, H., Pei, Z., Mao, H., Ying, J., Li, S., Ma, X., Liu, B., Mao, F., and Gong, W.: Quantifying facility-scale CO_2 emissions using spaceborne hyperspectral imageries, Remote Sens. Environ., 342, 115478, https://doi.org/10.1016/j.rse.2026.115478, 2026.

Han, G., Zhang, H., Huang, Y., Chen, W., Mao, H., Zhang, X., Ma, X., Li, S., Zhang, H., and Liu, J.: First global XCO_2 observations fromspaceborne lidar: methodology and initial result, Remote Sens. Environ., 330, 114954, https://doi.org/10.1016/j.rse.2025.114954, 2025.

Hersbach, H., Bell, B., Berrisford, P., Biavati, G., Horányi, A., Muñoz Sabater, J., Nicolas, J., Peubey, C., Radu, R., and Rozum, I.: The ERA5 global reanalysis, Q. J. Roy. Meteorol. Soc., 146, 1999–2049, https://doi.org/10.1002/qj.3803, 2023.

Huang, T., Zhu, X., Zhong, Q., Yun, X., Meng, W., Li, B., Ma, J., Zeng, E. Y., and Tao, S.: Spatial and temporal trends in global emissions of nitrogen oxides from 1960 to 2014, Environ. Sci. Technol., 51, 7992–8000, 2017.

Huang, Y., Han, G., Shi, T., Li, S., Mao, H., Nie, Y., and Gong, W.: Fi-scape: a divergence theorem based emission quantification model for air/space-borne imaging spectrome-

ter derived xCH_4 observations, IEEE J-STARS, 18, 255–272, https://doi.org/10.1109/JSTARS.2024.3490896, 2024.

Huang, Y., Han, G., Yi, J., Shi, T., Zhang, Y., Luo, H., Mao, H., Li, S., Mao, F., and Gong, W.: Rapid methane flux estimation combining MethaneSAT and Sentinel-5P observations: A case study of Turkmenistan, Geophys. Res. Lett., 52, e2025GL119369, https://doi.org/10.1029/2025GL119369, 2025.

Jöckel, P., Tost, H., Pozzer, A., Kunze, M., Kirner, O., Brenninkmeijer, C. A. M., Brinkop, S., Cai, D. S., Dyroff, C., Eckstein, J., Frank, F., Garny, H., Gottschaldt, K.-D., Graf, P., Grewe, V., Kerkweg, A., Kern, B., Matthes, S., Mertens, M., Meul, S., Neumaier, M., Nützel, M., Oberländer-Hayn, S., Ruhnke, R., Runde, T., Sander, R., Scharffe, D., and Zahn, A.: Earth System Chemistry integrated Modelling (ESCiMo) with the Modular Earth Submodel System (MESSy) version 2.51, Geosci. Model Dev., 9, 1153–1200, https://doi.org/10.5194/gmd-9-1153-2016, 2016.

Kiemle, C., Ehret, G., Amediek, A., Fix, A., Quatrevalet, M., and Wirth, M.: Potential of spaceborne lidar measurements of carbon dioxide and methane emissions from strong point sources, Remote Sens-Basel, 9, 1137, https://doi.org/10.3390/rs9111137, 2017.

Koene, E. F. M., Brunner, D., and Kuhlmann, G.: On the theory of the divergence method for quantifying source emissions from satellite observations, J. Geophys. Res.-Atmos., 129, e2023JD039904, https://doi.org/10.1029/2023JD039904, 2024.

Konovalov, I. B., Berezin, E. V., Ciais, P., Broquet, G., Zhuravlev, R. V., and Janssens-Maenhout, G.: Estimation of fossil-fuel CO_2 emissions using satellite measurements of "proxy" species, Atmos. Chem. Phys., 16, 13509–13540, https://doi.org/10.5194/acp-16-13509-2016, 2016.

Le Quéré, C., Andrew, R. M., Friedlingstein, P., Sitch, S., Hauck, J., Pongratz, J., Pickers, P. A., Korsbakken, J. I., Peters, G. P., Canadell, J. G., Arneth, A., Arora, V. K., Barbero, L., Bastos, A., Bopp, L., Chevallier, F., Chini, L. P., Ciais, P., Doney, S. C., Gkritzalis, T., Goll, D. S., Harris, I., Haverd, V., Hoffman, F. M., Hoppema, M., Houghton, R. A., Hurtt, G., Ilyina, T., Jain, A. K., Johannessen, T., Jones, C. D., Kato, E., Keeling, R. F., Goldewijk, K. K., Landschützer, P., Lefèvre, N., Lienert, S., Liu, Z., Lombardozzi, D., Metzl, N., Munro, D. R., Nabel, J. E. M. S., Nakaoka, S., Neill, C., Olsen, A., Ono, T., Patra, P., Peregon, A., Peters, W., Peylin, P., Pfeil, B., Pierrot, D., Poulter, B., Rehder, G., Resplandy, L., Robertson, E., Rocher, M., Rödenbeck, C., Schuster, U., Schwinger, J., Séférian, R., Skjelvan, I., Steinhoff, T., Sutton, A., Tans, P. P., Tian, H., Tilbrook, B., Tubiello, F. N., van der Laan-Luijkx, I. T., van der Werf, G. R., Viovy, N., Walker, A. P., Wiltshire, A. J., Wright, R., Zaehle, S., and Zheng, B.: Global Carbon Budget 2018, Earth Syst. Sci. Data, 10, 2141–2194, https://doi.org/10.5194/essd-10-2141-2018, 2018.

Li, H., Liu, B., Gong, W., Ma, Y., Jin, S., Wang, W., Fan, R., and Jiang, S.: Influence of clouds on planetary boundary layer height: A comparative study and factors analysis, Atmos. Res., 314, 107784, https://doi.org/10.1016/j.atmosres.2024.107784, 2025.

Lin, J. and Gerbig, C.: Accounting for the effect of transport errors on tracer inversions, Geophys. Res. Lett., 32, https://doi.org/10.1029/2004GL021127, 2005.

Liu, F., Duncan, B. N., Krotkov, N. A., Lamsal, L. N., Beirle, S., Griffin, D., McLinden, C. A., Goldberg, D. L., and Lu, Z.: A methodology to constrain carbon dioxide emissions from coal-fired power plants using satellite observations of co-emitted nitrogen dioxide, Atmos. Chem. Phys., 20, 99–116, https://doi.org/10.5194/acp-20-99-2020, 2020.

Liu, F., Tao, Z., Beirle, S., Joiner, J., Yoshida, Y., Smith, S. J., Knowland, K. E., and Wagner, T.: A new method for inferring city emissions and lifetimes of nitrogen oxides from high-resolution nitrogen dioxide observations: a model study, Atmos. Chem. Phys., 22, 1333–1349, https://doi.org/10.5194/acp-22-1333-2022, 2022.

Liu, M., Van Der A, R., Van Weele, M., Eskes, H., Lu, X., Veefkind, P., De Laat, J., Kong, H., Wang, J., and Sun, J.: A new divergence method to quantify methane emissions using observations of Sentinel-5P TROPOMI, Geophys. Res. Lett., 48, e2021GL094151, https://doi.org/10.1029/2021GL094151, 2021.

Lu, L., Cohen, J. B., Qin, K., Tiwari, P., Hu, W., Gao, H., and Zheng, B.: New Perspective on Using Observational Uncertainty to Improve Reliability of NO_x Emissions Over Northern China, IEEE T. Geosci. Remote, 63, 1–15, https://doi.org/10.1109/TGRS.2025.3620116, 2025.

Luo, B., Yang, J., Shi, S., Gan, R., Wu, Z., Wang, S., Wang, A., Du, L., and Gong, W.: InceptionFormer: A deep learning framework for UAV LiDAR point cloud completion to improve tree parameters estimation in dense forests, Remote Sens. Environ., 338, 115348, https://doi.org/10.1016/j.rse.2026.115348, 2026.

Miller, J. B., Tans, P. P., and Gloor, M.: Steps for success of OCO-2, Nat. Geosci., 7, 691–691, 2014.

National Centers for Environmental Prediction/National Weather Service/NOAA/U.S. Department of Commerce: NCEP FNL Operational Model Global Tropospheric Analyses, continuing from July 1999, NSF National Center for Atmospheric Research, https://doi.org/10.5065/D6M043C6, 2000 (updated daily).

National Centers for Environmental Prediction/National Weather Service/NOAA/U.S. Department of Commerce: NCEP GDAS/FNL 0.25 Degree Global Tropospheric Analyses and Forecast Grids, NSF National Center for Atmospheric Research [data set], https://doi.org/10.5065/D65Q4T4Z, 2015 (updated daily).

Oda, T., Bun, R., Kinakh, V., Topylko, P., Halushchak, M., Marland, G., Lauvaux, T., Jonas, M., Maksyutov, S., and Nahorski, Z.: Errors and uncertainties in a gridded carbon dioxide emissions inventory, Mitig.Adapt. Strat. Gl., 24, 1007–1050, 2019.

Pei, Z., Han, G., Ma, X., Shi, T., and Gong, W.: A method for estimating the background column concentration of CO_2 using the lagrangian approach, IEEE T. Geosci. Remote, 60, 1–12, 2022.

Qin, K., Lu, L., Liu, J., He, Q., Shi, J., Deng, W., Wang, S., and Cohen, J. B.: Model-free daily inversion of NO_x emissions using TROPOMI (MCMFE-NO_x) and its uncertainty: Declining regulated emissions and growth of new sources, Remote Sens. Environ., 295, 113720, https://doi.org/10.1016/j.rse.2023.113720, 2023.

Qu, C., Wang, W., Wu, Z., Wang, L., Liu, K., Wu, L., and Miao, Z.: Zero-Shot Vision-Language Model for Rapid Damaged Bridge Extraction in Emergency Response: A Case Study of the 2025 Myanmar Earthquake, IEEE Geosci. Remote S., 23, 021127, https://doi.org/10.1109/LGRS.2026.3673614, 2026.

Refaat, T. F., Singh, U. N., Yu, J., Petros, M., Remus, R., and Ismail, S.: Double-pulse 2-ìm integrated path differential absorption lidar airborne validation for atmospheric carbon dioxide measurement, Appl. Optics, 55, 4232–4246, 2016.

Reuter, M., Buchwitz, M., Schneising, O., Krautwurst, S., O'Dell, C. W., Richter, A., Bovensmann, H., and Burrows, J. P.: Towards monitoring localized CO_2 emissions from space: co-located regional CO_2 and NO_2 enhancements observed by the OCO-2 and S5P satellites, Atmos. Chem. Phys., 19, 9371–9383, https://doi.org/10.5194/acp-19-9371-2019, 2019.

Rey-Pommier, A., Chevallier, F., Ciais, P., Christoudias, T., Kushta, J., Georgiou, G., Violaris, A., Dubart, F., and Sciare, J.: Mapping NO_x emissions in Cyprus using TROPOMI observations: evaluation of the flux-divergence scheme using multiple parameter sets, Environ. Sci. Pollut. R., 32, 1932–1951, 2025.

Schwandner, F. M., Gunson, M. R., Miller, C. E., Carn, S. A., Eldering, A., Krings, T., Verhulst, K. R., Schimel, D. S., Nguyen, H. M., and Crisp, D.: Spaceborne detection of localized carbon dioxide sources, Science, 358, eaam5782, https://doi.org/10.1126/science.aam5782, 2017.

Sheng, M., Hou, Y., Song, H., Ye, X., Lei, L., Ma, P., and Zeng, Z.-C.: Estimating anthropogenic CO_2 emissions from China's Yangtze River Delta using OCO-2 observations and WRF-Chem simulations, Remote Sens. Environ., 316, 114515, https://doi.org/10.1016/j.rse.2024.114515, 2025.

Sun, K.: Derivation of emissions from satellite-observed column amounts and its application to TROPOMI NO_2 and CO observations, Geophys. Res. Lett., 49, e2022GL101102, https://doi.org/10.1029/2022GL101102, 2022.

Sun, K., Li, L., Jagini, S., and Li, D.: A satellite-data-driven framework to rapidly quantify air-basin-scale NOx emissions and its application to the Po Valley during the COVID-19 pandemic, Atmos. Chem. Phys., 21, 13311–13332, https://doi.org/10.5194/acp-21-13311-2021, 2021.

Sun, K., Zhu, L., Cady-Pereira, K., Chan Miller, C., Chance, K., Clarisse, L., Coheur, P.-F., González Abad, G., Huang, G., Liu, X., Van Damme, M., Yang, K., and Zondlo, M.: A physics-based approach to oversample multi-satellite, multispecies observations to a common grid, Atmos. Meas. Tech., 11, 6679–6701, https://doi.org/10.5194/amt-11-6679-2018, 2018a.

Sun, Y., Frankenberg, C., Jung, M., Joiner, J., Guanter, L., Köhler, P., and Magney, T.: Overview of Solar-Induced chlorophyll Fluorescence (SIF) from the Orbiting Carbon Observatory-2: Retrieval, cross-mission comparison, and global monitoring for GPP, Remote Sens. Environ., 209, 808–823, 2018b.

Team, M.: The Multi-resolution Emission Inventory Model for Climate and Air Pollution Research, MEIC Model, http://meicmodel.org.cn/?page_id=2351&lang=en#firstPage (last access: 29 January 2026), 2012.

van Geffen, J., Eskes, H., Compernolle, S., Pinardi, G., Verhoelst, T., Lambert, J.-C., Sneep, M., ter Linden, M., Ludewig, A., Boersma, K. F., and Veefkind, J. P.: Sentinel-5P TROPOMI NO_2 retrieval: impact of version v2.2 improvements and comparisons with OMI and ground-based data, Atmos. Meas. Tech., 15, 2037–2060, https://doi.org/10.5194/amt-15-2037-2022, 2022.

Veefkind, J. P., Aben, I., McMullan, K., Förster, H., De Vries, J., Otter, G., Claas, J., Eskes, H., De Haan, J., and Kleipool, Q.: TROPOMI on the ESA Sentinel-5 Precursor: A GMES mission for global observations of the atmospheric composition for climate, air quality and ozone layer applications, Remote Sens. Environ., 120, 70–83, 2012.

Verhoelst, T., Compernolle, S., Pinardi, G., Lambert, J.-C., Eskes, H. J., Eichmann, K.-U., Fjæraa, A. M., Granville, J., Niemeijer, S., Cede, A., Tiefengraber, M., Hendrick, F., Pazmiño, A., Bais, A., Bazureau, A., Boersma, K. F., Bognar, K., Dehn, A., Donner, S., Elokhov, A., Gebetsberger, M., Goutail, F., Grutter de la Mora, M., Gruzdev, A., Gratsea, M., Hansen, G. H., Irie, H., Jepsen, N., Kanaya, Y., Karagkiozidis, D., Kivi, R., Kreher, K., Levelt, P. F., Liu, C., Müller, M., Navarro Comas, M., Piters, A. J. M., Pommereau, J.-P., Portafaix, T., Prados-Roman, C., Puentedura, O., Querel, R., Remmers, J., Richter, A., Rimmer, J., Rivera Cárdenas, C., Saavedra de Miguel, L., Sinyakov, V. P., Stremme, W., Strong, K., Van Roozendael, M., Veefkind, J. P., Wagner, T., Wittrock, F., Yela González, M., and Zehner, C.: Ground-based validation of the Copernicus Sentinel-5P TROPOMI NO_2 measurements with the NDACC ZSL-DOAS, MAX-DOAS and Pandonia global networks, Atmos. Meas. Tech., 14, 481–510, https://doi.org/10.5194/amt-14-481-2021, 2021.

Wang, R., Tao, S., Ciais, P., Shen, H. Z., Huang, Y., Chen, H., Shen, G. F., Wang, B., Li, W., Zhang, Y. Y., Lu, Y., Zhu, D., Chen, Y. C., Liu, X. P., Wang, W. T., Wang, X. L., Liu, W. X., Li, B. G., and Piao, S. L.: High-resolution mapping of combustion processes and implications for CO_2 emissions, Atmos. Chem. Phys., 13, 5189–5203, https://doi.org/10.5194/acp-13-5189-2013, 2013.

Wang, S., Cohen, J. B., Guan, L., Lu, L., Tiwari, P., and Qin, K.: Observationally constrained global NO_x and CO emissions variability reveals sources which contribute significantly to CO_2 emissions, npj Climate and Atmospheric Science, 8, 87, https://doi.org/10.1038/s41612-025-00977-2, 2025.

Wei, C.: Historical trend and drivers of China's CO_2 emissions from 2000 to 2020, Environ. Dev. Sustain., 26, 2225–2244, 2024.

Wu, D., Lin, J. C., Fasoli, B., Oda, T., Ye, X., Lauvaux, T., Yang, E. G., and Kort, E. A.: A Lagrangian approach towards extracting signals of urban CO_2 emissions from satellite observations of atmospheric column CO_2 (XCO_2): X-Stochastic Time-Inverted Lagrangian Transport model ("X-STILT v1"), Geosci. Model Dev., 11, 4843–4871, https://doi.org/10.5194/gmd-11-4843-2018, 2018.

Xing, Y., Han, G., Mao, H., He, H., Bo, Z., Gong, R., Ma, X., and Gong, W.: MAM-YOLOv9: A Multi-Attention Mechanism Network for Methane Emission Facility Detection in High-Resolution Satellite Remote Sensing Images, IEEE T. Geosci. Remote, 63, 5614516, https://doi.org/10.1109/TGRS.2025.3545034, 2025.

Xu, J., Guan, Y., Oldfield, J., Guan, D., and Shan, Y.: China carbon emission accounts 2020–2021, Appl. Energ., 360, 122837, https://doi.org/10.1016/j.apenergy.2024.122837, 2024.

Xu, M., Han, G., Pei, Z., Yu, H., Li, S., and Gong, W.: Advanced method for compiling a high-resolution gridded anthropogenic CO_2 emission inventory at a regional scale, Geo-spatial Information Science, 28, 117–130, 2025a.

Xu, T., Zhang, C., and Liu, C.: Enhanced quantification of global carbon emitters using collocated OCO-3 CO_2 and NO_2 observations from twin polar-orbiting satellites, Geophys. Res. Lett., 52, e2025GL116877, 2025b.

Yang, E. G., Kort, E. A., Ott, L. E., Oda, T., and Lin, J. C.: Using space-based CO_2 and NO_2 observations to estimate urban CO_2 emissions, J. Geophys. Res.-Atmos., 128, e2022JD037736, https://doi.org/10.1029/2022JD037736, 2023.

Ye, X., Lauvaux, T., Kort, E. A., Oda, T., Feng, S., Lin, J. C., Yang, E. G., and Wu, D.: Constraining fossil fuel CO_2 emissions from urban area using OCO-2 observations of total column CO_2, J. Geophys. Res.-Atmos., 125, e2019JD030528, https://doi.org/10.1029/2019JD030528, 2020.

Yi, J., Huang, Y., Pei, Z., and Han, G.: Urban Area Observing System (UAOS) simulation experiment using DQ-1 total column concentration observations, Atmos. Chem. Phys., 25, 13687–13710, https://doi.org/10.5194/acp-25-13687-2025, 2025a.

Yi, J., Huang, Y., Pei, Z., and Han, G.: Urban Area Observing System (UAOS) simulation experiment using DQ-1 total column concentration observations, Atmos. Chem. Phys., 25, 13687–13710, https://doi.org/10.5194/acp-25-13687-2025, 2025b.

Zhang, H., Han, G., Ma, X., Chen, W., Zhang, X., Liu, J., and Gong, W.: Robust algorithm for precise X CO 2 retrieval using single observation of IPDA LIDAR, Opt. Express, 31, 11846–11863, 2023.

Zhang, H., Han, G., Chen, W., Pei, Z., Liu, B., Liu, J., Zhang, T., Li, S., and Gong, W.: Validation Method for Spaceborne IPDA LIDAR X_{CO_2} Products via TCCON, IEEE J-STARS, 17, 16984–16992, 2024.

Zhang, Q., Boersma, K. F., Zhao, B., Eskes, H., Chen, C., Zheng, H., and Zhang, X.: Quantifying daily NO_x and CO_2 emissions from Wuhan using satellite observations from TROPOMI and OCO-2, Atmos. Chem. Phys., 23, 551–563, https://doi.org/10.5194/acp-23-551-2023, 2023.

Zhang, X., Yang, H., Bu, L., Fan, Z., Xiao, W., Chen, B., Zhang, L., Liu, S., Wang, Z., Liu, J., Chen, W., and Lee, X.: Estimation of diurnal emissions of CO_2 from thermal power plants using spaceborne integrated path differential absorption (IPDA) lidar, Atmos. Chem. Phys., 25, 6725–6740, https://doi.org/10.5194/acp-25-6725-2025, 2025.

Zhang, Y., Han, G., Huang, Y., Wang, H., Zhang, H., Pei, Z., Pu, Y., Luo, H., Yi, J., and Shi, T.: Attributing GHG emissions to individual facilities using multi-temporal hyperspectral images: Methodology and applications, ISPRS J. Photogramm., 232, 937–956, 2026.

Zheng, B., Geng, G., Ciais, P., Davis, S. J., Martin, R. V., Meng, J., Wu, N., Chevallier, F., Broquet, G., and Boersma, F.: Satellite-based estimates of decline and rebound in China's CO_2 emissions during COVID-19 pandemic, Science Advances, 6, eabd4998, https://doi.org/10.1126/sciadv.abd4998, 2020.